

The Seoul National University AGN Monitoring Project III: H β lag measurements of 32 luminous AGNs and the high-luminosity end of the size-luminosity relation

JONG-HAK WOO,¹ SHU WANG,¹ SUVENDU RAKSHIT,^{1,2} HOJIN CHO,¹ DONGHOON SON,¹ VARDHA N. BENNETT,³ ELENA GALLO,⁴ EDMUND HODGES-KLUCK,^{5,4} TOMMASO TREU,⁶ AARON J. BARTH,⁷ WANJIN CHO,¹ ADI FOORD,⁸ JAEHYUK GEUM,⁹ HENGXIAO GUO,^{10,7} YASHASHREE JADHAV,¹ YISEUL JEON,¹ KYLE M. KABASARES,⁷ WON-SUK KANG,¹¹ CHANGSEOK KIM,¹ MINJIN KIM,⁹ TAE-WOO KIM,^{11,12} HUYNH ANH N. LE,^{1,13} MATTHEW A. MALKAN,⁶ AMIT KUMAR MANDAL,¹ DAESEONG PARK,^{14,9} CHANCE SPENCER,³ JAEJIN SHIN,^{1,9,14} HYUN-IL SUNG,¹⁴ VIVIAN U,⁷ PETER R. WILLIAMS,⁶ AND NICK YEE³

¹*Department of Physics & Astronomy, Seoul National University, Seoul 08826, Republic of Korea, jhwoo@snu.ac.kr, wangshu100002@gmail.com*

²*Aryabhatta Research Institute of Observational Sciences, Manora Peak, Nainital-263001, Uttarakhand, India*

³*Physics Department, California Polytechnic State University, San Luis Obispo, CA 93407, USA*

⁴*Department of Astronomy, University of Michigan, Ann Arbor, MI 48109, USA*

⁵*NASA/GSFC, Code 662, Greenbelt, MD 20771, USA*

⁶*Department of Physics and Astronomy, University of California, Los Angeles, CA 90095-1547, USA*

⁷*Department of Physics and Astronomy, 4129 Frederick Reines Hall, University of California, Irvine, CA, 92697-4575, USA*

⁸*Kavli Institute of Particle Astrophysics and Cosmology, Stanford University, Stanford, CA 94305, USA*

⁹*Major in Astronomy and Atmospheric Sciences, Kyungpook National University, Daegu 41566, Republic of Korea*

¹⁰*Key Laboratory for Research in Galaxies and Cosmology, Shanghai Astronomical Observatory, Chinese Academy of Sciences, 80 Nandan Road, Shanghai 200030, People's Republic of China*

¹¹*National Youth Space Center, Goheung 59567, Republic of Korea*

¹²*Department of Astronomy and Space Science, Chungbuk National University, Cheongju 28644, Republic of Korea*

¹³*CAS Key Laboratory for Research in Galaxies and Cosmology, Department of Astronomy, University of Science and Technology of China, Hefei 230026, China*

¹⁴*Korea Astronomy and Space Science Institute, Daejeon 34055, Republic of Korea*

ABSTRACT

We present the main results from a long-term reverberation mapping campaign carried out for the Seoul National University Active Galactic Nuclei (AGN) Monitoring Project. High-quality data were obtained during 2015-2021 for 32 luminous AGNs (i.e., continuum luminosity in the range of 10^{44-46} erg s^{-1}) at a regular cadence, of 20-30 days for spectroscopy and 3-5 days for photometry. We obtain time lag measurements between the variability in the H β emission and the continuum for 32 AGNs; twenty-five of those have the best lag measurements based on our quality assessment, examining correlation strength, and the posterior lag distribution. Our study significantly increases the current sample of reverberation-mapped AGNs, particularly at the moderate to high luminosity end. Combining our results with literature measurements, we derive a H β broad line region size-luminosity relation with a shallower slope than reported in the literature. For a given luminosity, most of our measured lags are shorter than the expectation, implying that single-epoch black hole mass estimators based on previous calibrations could suffer large systematic uncertainties.

Keywords: quasars: general — quasars: emission lines — galaxies

1. INTRODUCTION

Black hole mass (M_{BH}) is a key parameter in understanding the physics of active galactic nuclei (AGN) and the connection of black hole growth with galaxy evolution. M_{BH} can be determined based on the spatially resolved data by measuring the kinematics of stars, gas, and masers near the sphere of influence of supermassive black holes (e.g., Gültekin et al. 2009; Barth et al. 2001;

Marconi et al. 2003; Davies et al. 2006; Scharwächter et al. 2013; den Brok et al. 2015; Boizelle et al. 2021; Kabasares et al. 2022), or by imaging black hole shadows along with theoretical approach (Event Horizon Telescope Collaboration et al. 2019, 2022). However, these methods are limited to relatively nearby objects due to the limited spatial resolution of current facilities.

In contrast, reverberation mapping (RM; [Blandford & McKee 1982](#); [Peterson 1993](#)) based on the variability of AGNs can be applied to mass-accreting black holes beyond the local universe. Currently, the RM technique and related indirect mass estimators are the primary methods for determining M_{BH} over a large range of cosmic time. The main idea of RM is to measure the time delay (τ) between the flux variations of the continuum and broad emission lines, which represents the light travel time from the central photo-ionizing source to the photo-ionized gas, providing the size (or radius) of the broad-line region (BLR). Based on the virial assumption that the dynamics of gas in the BLR is governed by the gravitational potential of the central black hole, M_{BH} is determined by combining the measured size (R_{BLR}) with the velocity measure (V) from the width of broad emission lines as:

$$M_{\text{BH}} = f \frac{(c\tau)V^2}{G}, \quad (1)$$

where c is the speed of light, G is the gravitational constant and f is a factor representing the unknown geometry of the BLR. While f can be different for each AGN, an average f factor is calibrated based on the black hole mass - stellar velocity dispersion relation of the local galaxies (e.g., [Onken et al. 2004](#); [Woo et al. 2010](#); [Park et al. 2012a](#); [Woo et al. 2015](#)). Note that the f factor is the main source of the uncertainty of M_{BH} , up to 0.4 dex in the case of $\text{H}\beta$ reverberation based M_{BH} ([Park et al. 2012a](#); [Woo et al. 2015](#)). The f factor has been constrained for a small number of individual AGNs based on the dynamical modeling of the BLR combined with the velocity-resolved reverberation-mapping data (e.g., [Pancoast et al. 2011, 2014a,b](#); [Li et al. 2014](#); [Williams et al. 2018](#); [Villafañã et al. 2022](#)).

Early studies of RM reported a correlation between the measured $\text{H}\beta$ BLR size and the monochromatic continuum luminosity at 5100\AA (L_{5100}) ([Wandel et al. 1999](#); [Kaspi et al. 2000](#)), opening an indirect way of estimating BLR size and M_{BH} from single-epoch spectra since monitoring data for RM is not required (e.g., [Woo & Urry 2002](#); [Vestergaard & Peterson 2006](#); [Shen et al. 2011](#); [Shen & Liu 2012](#); [Dalla Bontà et al. 2020](#)). While the best-fit slope was initially reported as 0.7 ([Kaspi et al. 2000](#)), following studies based on HST images calibrated the slope as ~ 0.5 as expected from photoionization after correcting for the host galaxy contribution to the observed L_{5100} , particularly for low-luminosity AGNs with relatively strong stellar continuum (e.g., [Bentz et al. 2009a, 2013](#)).

It is of importance to investigate the photoionization and the BLR size-luminosity relation for a general population of AGNs over a large dynamic range of M_{BH}

and AGN luminosity. In the past, however, RM studies were limited to low-to-moderate luminosity AGNs due to the observational challenges. The main difficulty is that long-term spectroscopic monitoring with good cadence is required to obtain an accurate time lag measurement between AGN continuum and emission line flux variations. Over the last decades, a number of intensive programs were dedicated to RM studies, dramatically increasing the sample size and the dynamic range of the reverberation-mapped AGNs ([Barth et al. 2015](#); [Du et al. 2015](#); [Grier et al. 2017](#); [Zhang et al. 2019](#); [U et al. 2022](#); [Malik et al. 2022](#)). However, it is still important to extend the RM study to more luminous AGNs, particularly in the high-luminosity regime (i.e., $L_{5100} = 10^{45\sim 46} \text{ erg s}^{-1}$), which are the representative luminosity of high- z AGNs. For example, an AGN with $L_{5100} = 10^{46}$ at $z=1$ is expected to have a $\text{H}\beta$ time lag of 500-600 days in the observed-frame, which then has to be determined based on a monitoring campaign of 5-10 years. Such a long timeline explains why there is a relative lack of very luminous AGNs among the reverberation-mapped AGNs (see Figure 1).

Currently, the $\text{H}\beta$ time lag has been reported for more than 200 AGNs (e.g., [Wandel et al. 1999](#); [Kaspi et al. 2000](#); [Peterson et al. 2004](#); [Bentz et al. 2009b, 2013](#); [Barth et al. 2015](#); [Grier et al. 2017](#); [Park et al. 2017](#); [Du & Wang 2019](#); [Zhang et al. 2019](#); [Martínez-Aldama et al. 2019](#); [Dalla Bontà et al. 2020](#); [Hu et al. 2021](#); [Li et al. 2021](#); [U et al. 2022](#); [Malik et al. 2022](#)). These AGNs show a larger scatter in the $\text{H}\beta$ BLR size-luminosity relation compared to the previously reported relations (e.g., [Bentz et al. 2013](#)). While it is possible that the intrinsic scatter may not be larger than previously thought, a consistent study of cross-correlations with uniform measurements of $\text{H}\beta$ lag and uncertainty is required to properly constrain the intrinsic scatter as well as the slope of the size-luminosity relation. Note that various studies performed by different groups adopted different criteria to select reliable lag measurements and inconsistent methods to derive the uncertainty of the lag.

In particular, AGNs with a super-Eddington ratio seem to deviate from the size-luminosity relation according to the results from the recent project, the Super Eddington Accreting Massive BHs (SEAMBHs) ([Wang et al. 2014](#); [Du et al. 2014](#); [Zhang et al. 2019](#); [Hu et al. 2021](#); [Li et al. 2021](#)). It is claimed that the deviation from the size-luminosity relation correlates with the accretion rate or the flux ratios between Fe II and $\text{H}\beta$ (R_{Fe}) or between [O III] and $\text{H}\beta$ lines. This systematic trend is crucial to verify since it will introduce strong bias in M_{BH} determination for high Eddington ratio AGNs

from single-epoch spectra (see the discussion by Li et al. 2021).

To extend the RM study to moderate-to-high luminosity AGNs and investigate the $H\beta$ BLR size-luminosity relation at the high-luminosity end, we performed an intensive long-term campaign, the Seoul National University AGN Monitoring Project (SAMP). Using a 100 AGNs with moderate to high luminosity ($L_{5100} > 10^{44.0}$ erg s^{-1}) out to $z < 0.4$, we started test photometry in 2015. Then, we carried out photometric and spectroscopic monitoring with the Lick 3-m, MDM 2.4-m and other 1-m class telescopes until the middle of 2021. The project strategy and sample selection were presented by Woo et al. (2019, hereafter Paper I), and initial measurements of the $H\beta$ lag for two targets based on the first three-year data were reported by Rakshit et al. (2019). In this work, we present the final sample of 32 AGNs from the six-year spectroscopic campaign and the $H\beta$ lag analysis. The measurements of $H\alpha$ lag are presented by Cho et al. (2023), and the photometry monitoring results of 72 AGNs will be presented by Son et al. (in preparation). We briefly describe the sample selection in Section 2 and data analysis in Section 3. Results and discussion are presented in Sections 4 and 5, respectively, followed by Discussion in Section 5 and Summary in Section 6. Throughout this paper, we use the Λ CDM cosmology, with $H_0 = 72.0$ km s^{-1} Mpc $^{-1}$, and $\Omega_m = 0.3$.

2. OBSERVATIONS AND DATA REDUCTION

2.1. Sample

We selected the best available type 1 AGNs for a multi-year monitoring program for our facilities, by considering the expected lag, observability, and feasibility of $H\beta$ lag measurements along with the simulation of light curves and spectral decomposition. The details of the project strategy and sample selection of the SAMP were presented by Woo et al. (2019), and here we briefly describe the sample.

We selected relatively high-luminosity AGNs using the MILLIQUAS catalog (Milliquas v4.5 (2015) update, Flesch 2015; Boroson & Green 1992), in order to test the high-end of the $H\beta$ BLR size-luminosity relation. As summarized by Woo et al. (2019), we initially selected 100 AGNs with the V -band magnitude < 17.0 at $z < 0.5$. The $H\beta$ lag is expected to range from ~ 40 to ~ 250 days in the observed-frame, which is estimated based on the monochromatic continuum luminosity at 5100\AA (L_{5100}) and the size-luminosity relation of Bentz et al. (2013). In this process, we used SDSS spectra or the spectra provided by Boroson & Green (1992) to measure $\lambda L_{\lambda}(5100\text{\AA})$. B -band photometry is used instead if there is no available spectrum. We identified 48

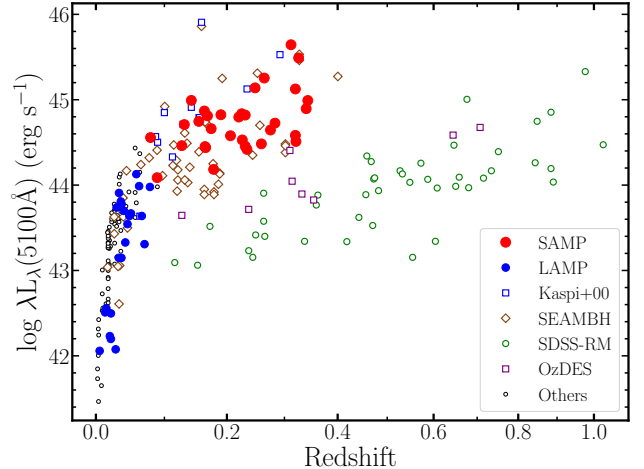


Figure 1. Luminosity and redshift distribution of the SAMP final sample (red filled circles) compared to the $H\beta$ lag measured AGNs in other RM campaigns, including the LAMP 2008 and 2016 (Bentz et al. 2009b; U et al. 2022), the monitoring campaign of PG quasars by Kaspi et al. (2000), the SEAMBHs (Du et al. 2014; Wang et al. 2014; Du et al. 2015, 2016, 2018a; Zhang et al. 2019; Hu et al. 2021; Li et al. 2021), OzDES (Malik et al. 2022), the SDSS-RM (Grier et al. 2017), and other AGNs in the collection by Dalla Bontà et al. (2020).

AGNs with an expected lag longer than 70 days in the initial sample as the first priority targets (i.e., SAMP ID started with Pr1 in Table 1) and 37 AGNs with an expected lag shorter than 70 days as the second priority targets (i.e., SAMP ID started with Pr2). We also included 15 PG QSOs (Boroson & Green 1992) for filling up the seasonal gaps and increasing the sample size (i.e., SAMP ID started with P). These PG QSOs are also medium-to-high luminosity objects with an expected lag of ~ 50 -300 days.

Using the initial sample of 100 AGNs, we performed the variability test of continuum and $H\beta$ line emission based on photometry and spectroscopy during the first few years, and excluded weakly-varying objects. Based on these variability check processes, we continued 6-year monitoring for a final sample of 32 AGNs. This final AGNs are out to $z \sim 0.4$ with luminosity $L_{5100} > 10^{44}$ erg s^{-1} as presented in Figure 1. We emphasize that the SAMP final sample covers relatively higher luminosity ranges compared to previous $H\beta$ monitoring campaigns (e.g., Kaspi et al. 2000; Bentz et al. 2009b; Barth et al. 2015; Wang et al. 2014; Du et al. 2014, 2015, 2016; Grier et al. 2017; U et al. 2022; Malik et al. 2022). The properties of the sample are summarized in Table 1.

2.2. Photometry

Table 1. Sample properties and observation parameters

Name	SDSS Identifier	z	m_V	A_V	PA	Exp.	S/N	Band	SAMPID	
(1)	(2)	(3)	(4)	(5)	(6)	(7)	(8)	(9)	(10)	
1	Mrk 1501	J001031.00+105829.4	0.089	15.8	0.273	Para	800	41	B, V	P02
2	PG 0026+129	J002913.70+131603.9	0.142	15.2	0.195	Para	600	73	B, V	P03
3	PG 0052+251	J005452.11+252539.0	0.154	15.7	0.129	Para	800	46	B, V	P06
4	J0101+422	J010131.17+422935.5	0.190	16.3	0.244	96.4	1200	46	B, V	Pr1_ID01
5	J0140+234	J014035.01+234451.1	0.320	17.0	0.362	67.1	1200	31	B, V	Pr1_ID03
6	Mrk 1014	J015950.25+002340.8	0.163	15.5	0.079	Para	800	39	B, V	P07
7	J0801+512	J080112.02+512812.0	0.321	18.4	0.136	90.5	3600	14	B, V	Pr1_ID11
8	J0939+375	J093939.69+375705.8	0.231	17.2	0.049	100.8	2400	27	B, V	Pr1_ID14
9	PG 0947+396	J095048.39+392650.4	0.206	16.7	0.053	161.8	1200	31	B, V	Pr1_ID15
10	J1026+523	J102613.90+523751.2	0.259	17.9	0.037	94.8	2400	16	B, V	Pr1_ID17
11	J1059+665	J105935.50+665757.9	0.340	17.4	0.042	67.9	2400	24	B, V	Pr1_ID18
12	PG 1100+772	J110413.87+765858.1	0.312	15.4	0.100	66.3	600	41	B, V	Pr1_ID19
13	J1105+671	J110527.25+671636.4	0.320	17.7	0.050	112.5	2400	23	V, R	Pr1_ID20
14	J1120+423	J112007.43+423551.3	0.226	17.2	0.051	72.7	2400	30	B, V	Pr1_ID23
15	PG 1121+422	J112439.18+420145.0	0.225	16.5	0.062	133.0	1200	33	B, V	Pr1_ID24
16	J1203+455	J120348.08+455951.1	0.343	17.2	0.045	158.2	2400	25	B, V	Pr1_ID26
17	PG 1202+281	J120442.10+275411.8	0.165	16.7	0.057	168.7	1800	30	B, V	Pr1_ID27
18	J1217+333	J121752.16+333447.2	0.178	17.3	0.037	169.9	2400	26	B, V	Pr1_ID29
19	VIII Zw 218	J125337.71+212618.2	0.127	15.9	0.139	126.2	1800	38	B, V	Pr1_ID30
20	PG 1322+659	J132349.52+654148.1	0.168	15.9	0.053	97.4	1200	39	B, V	Pr2_ID18
21	J1415+483	J141535.94+483543.6	0.275	17.6	0.040	192.9	3600	28	B, V	Pr1_ID36
22	PG 1427+480	J142943.07+474726.2	0.220	16.5	0.047	90.8	1800	38	B, V	Pr2_ID24
23	PG 1440+356	J144207.47+352622.9	0.079	14.6	0.039	157.1	600	70	B, V	Pr2_ID26
24	J1456+380	J145608.63+380038.5	0.283	17.1	0.030	55.4	1800	25	B, V	Pr1_ID38
25	J1526+275	J152624.02+275452.1	0.231	16.8	0.113	137.4	1800	43	B, V	Pr1_ID40
26	J1540+355	J154004.25+355050.1	0.164	16.7	0.071	8.10	1200	37	B, V	Pr1_ID41
27	PG 1545+210	J154743.53+205216.6	0.264	16.0	0.117	59.10	1200	41	B, V	Pr1_ID42
28	PG 1612+261	J161413.20+260416.2	0.131	15.4	0.151	17.2	600	56	B, V	Pr2_ID35
29	J1619+501	J161911.24+501109.2	0.234	16.0	0.055	46.70	1800	25	B, V	Pr1_ID43
30	J1935+531	J19352118+5314119 [†]	0.248	16.4	0.312	169.5	1200	34	B, V	Pr1_ID47
31	PG 2251+113	J225410.42+113638.8	0.326	15.8	0.236	Para	720	59	V, R	P13
32	PG 2349-014	J235156.12-010913.3	0.174	16.1	0.075	Para	1200	37	B, V	P15

Notes. Column (1): Object name in the sequence of R.A. with the sequence No. shown in the front. Column (2): SDSS identifier. Column (3): Redshift. Column (4): the median apparent V -band magnitudes measured from the SAMP light curves. Column (5): Extinction in V -band extracted from NED based on [Schlafly & Finkbeiner \(2011\)](#) dust map. Column (6): Slit position angle. The label Para means that the PA is set to be parallactic. Column (7): Typical exposure time of single-night spectroscopic observation. Column (8): Average signal-to-noise ratio per pixel of all spectra of this object. Column (9): Primary and secondary band in photometric observation. The primary band light curves are used as the continuum light curves. Column (10): Object ID defined for the project as used in Paper I.

[†] This object J1935+531 is not in the SDSS footprint. Its main identifier is 2MASS J19352118+5314119.

We performed photometric monitoring using several telescopes: the MDM 1.3-m and 2.4-m telescopes at the Kitt Peak, Tucson, Arizona, USA, the Lemmonsan Optical Astronomy Observatory (LOAO) 1-m telescope located on Mt. Lemmon, Tucson, Arizona, USA, the Lick observatory 1-m telescope located at Mt. Hamilton, California, USA, the Las Cumbres Observatory Global Telescope (LCOGT) network, and the Deokheung Optical Astronomy Observatory (DOAO) 1-m telescope. We used the B and V , or V and R band filters to monitor continuum variability, depending on the redshift of each object (see Table 1).

Details of the photometric data reduction and variability analysis including the final photometric light curves will be presented in a forthcoming paper (Son et al. in preparation). Here we briefly describe the basic information for completeness. We followed the standard reduction procedure for bias subtraction and flat-fielding using IRAF package (Tody 1986, 1993). We used the LA-Cosmic¹ task (van Dokkum 2001) to remove cosmic rays and adopted the Astrometry.net² (Lang et al. 2010) for astrometric calibration. Sub-exposure images were combined using the SWarp³ software (Bertin et al. 2002) by matching the position of all stars in the Field-of-View (FoV) of each image. We performed aperture photometry using the SExtractor⁴ software (Bertin & Arnouts 1996) with an initial aperture size to be 3 times of the seeing size. By generating the magnitude growth curve as a function of the aperture size, we tested whether the magnitude based on the seeing was fainter than the brightest magnitude in the growth curve, and enlarged the aperture size accordingly in order to avoid any aperture loss. A small fraction of images with bad quality due to the full moon, gust wind, or thick clouds were excluded from the final photometric light curves based on visual inspection of each image. We performed flux-calibration using non-variable stars in the FoV of each AGN, using the star catalogs of SDSS and APASS⁵. Finally, we obtained the photometric light curves of the sample in each band at each telescope.

We found systematic offset among the light curves obtained with different telescopes, presumably caused by various weather conditions and difference in the filter properties as often reported by previous studies (e.g., Peterson et al. 1995; Pancoast et al. 2019). Thus, it is critical to inter-calibrate these light curves in the

merging process. We performed the inter-calibration by adopting the python software PyCALI⁶ (Li et al. 2014) which used damped random walk (DRW) model to describe the AGN variability and determine the best scaling factors based on Bayesian statistics. For each AGN, we adopted the light curve from the MDM 1.3-m telescope as a reference, and aligned all the other light curves. Note that the MDM 1.3-m light curves have the largest number of epochs, which are also most evenly distributed over the monitoring time baseline. Systematic uncertainties were added to each telescope’s light curve during the inter-calibration process.

Visual inspection of the merged light curves showed that for most targets DOAO light curves were still relatively scattered and deviated from the general trend of the light curves obtained at other telescopes, presumably due to flux calibration issues, i.e., high humidity and quickly changing seeing condition at the DOAO observatory. In the case of the light curves obtained at the Lick 1-m and LCOGT telescopes, we sometimes found a similar problem for some objects. Under these circumstances, we decided to exclude the light curve from Lick 1-m and LCOGT as well.

We utilized the B -band light curve as the continuum light curves for all objects except for two higher redshift objects at $z > 0.3$, namely, J1105+671 and PG 2251+113, for which we instead adopted the V -band light curve. For seven AGNs, we found that the g -band light curves from the Zwicky Transient Facility (ZTF) were available, and combined them to the SAMP continuum light curves, in order to improve the temporal coverage and cadence. Note that ZTF is a time-domain survey, which started in 2018 and overlapped with the SAMP monitoring baseline. We used the ZTF DR8 to include the photometric data from March 2018 to September 2021. Following the previous studies based on the ZTF data (e.g., Sánchez-Sáez et al. 2021), we cleaned the ZTF light curves by requiring the `catflags` = 0, to avoid the effect of bad weather conditions (e.g., clouds, moon contamination, and large seeing). We assumed that the time lag between the B -band and ZTF g -band continuum fluxes is much smaller than that of $H\beta$ emission line as is the case according to the previous continuum reverberation studies (e.g., Jha et al. 2022; Netzer 2022). For example, Wang et al. (2023) reported that a typical size of the continuum emitting region is a factor of ~ 8 smaller than that of $H\beta$. By directly testing the lag between B and g -bands of our sample, we found that the lags between the two broadband light curves

¹ <http://www.astro.yale.edu/dokkum/lacosmic/>

² <http://astrometry.net>

³ <https://www.astromatic.net/software/swarp/>

⁴ <https://www.astromatic.net/software/extractor/>

⁵ www.aavso.org/apass

⁶ <https://github.com/LiyrAstroph/PyCALI>

were much smaller than the $H\beta$ time lags for the SAMP AGNs (Mandal et al. in preparation). By combining the SAMP and ZTF light curves, we obtained the improved light curves with better temporal coverage with a less than 3-day cadence, increasing the constraints of the continuum variability and the reliability of the lag measurements.

2.3. Spectroscopy

We carried out the spectroscopic monitoring using two telescopes, the Shane 3-m telescope at the Lick observatory and the 2.4-m telescope at the MDM observatory. For the Lick observations, we utilized the Kast double spectrograph⁷, which consists of two spectrographs, optimized for red and blue wavelength ranges, respectively. In this study, we focused on the $H\beta$ emission line and used only the red side of the observed spectra. We used the 600-line mm^{-1} grating, covering the spectral range of 4300–7100 Å and a dispersion of 2.33 Å pixel⁻¹ until September 2016. After the upgrade of the CCD in September 2016, the spectral range was changed to be 4450–7280 Å, and a dispersion of 1.27 Å pixel⁻¹. We used a 4'' slit width to minimize slit loss. Combined with the grating, Lick spectral setup provided a spectral resolution R of ~ 624 . We measured the instrumental resolution (FWHM) of 481 km s⁻¹ by utilizing unblended skylines. Calibration frames, i.e., bias, dome flats, and arc lamps (He, Ne, Ar, and Hg-Cd), were obtained at each night. For most objects, we used a fixed slit position angle (PA) for observations at airmass less than 1.3, while we adopted a parallactic angle for observations at higher airmass. The on-source exposure time of Lick observations was set between 360 and 1800 seconds depending on the magnitude of each target, in order to obtain a signal-to-noise ratio (S/N) per pixel > 15 -20 calculated over the entire spectral range.

For the MDM observations, we utilized the VPH blue grism with a spectral coverage of 3970 – 6870 Å and a dispersion of 0.715 Å pixel⁻¹. We used a 3'' slit width before February 2017, after which we ordered and replaced it with a customized 4'' slit, in order to make a consistent setup compared to the Lick spectroscopy. The corresponding instrumental resolution is $R = 617$. Calibration frames, including bias, dome flats, and Ar/Xe arc lamps were obtained at each night. The PA of slits was set to be the same as the Lick observations. The on-source exposure time of the MDM observations was set between 600 and 2400 seconds depending on the magnitude of target AGNs.

The sample of SAMP covers a large range of R.A., and individual targets show various levels of flux variability. To optimize the monitoring efficiency, we continuously checked the variability and the feasibility of the lag measurements based on the updated light curves in 1-2 month time scales. Note that we can predict strong variability of $H\beta$ line emission if we see a strong variability pattern in the photometric continuum light curves in advance. Thus, we reduced the time allocation of relatively non-varying targets, while we provided more spectroscopic time to promising targets, for which strong variability was detected in the photometric light curves. Consequently, cadence and the total observed number of epochs varied for each target. In Table 2 we summarize the observations of each object in the final sample.

We performed standard spectroscopic data reduction including overscan subtraction, bias, and flat-fielding using the standard IRAF package. The cosmic-ray rejection was done using the LA-Cosmic task. For the MDM spectra, we used a single sensitivity function, which was averaged over monitoring seasons, because the difference among various epochs was sufficiently small. In the case of the Lick calibration, we tested the consistency using individual sensitivity functions obtained at each night, which were constructed by fitting the spectra of spectrophotometric standard stars observed at each night (Oke 1990) with polynomial functions using a script provided by PyPeIt v1.4 (Prochaska et al. 2020a,b). We found that the results were almost consistent with those from the analysis with the IRAF, but provided better consistency at the edge of the spectral range, especially for 2017-2021 observations. Thus, we adopted the PyPeIt-reduced spectra for the data obtained in 2017-2021. For the 2016 data, the individual sensitivity function could not be accurately constrained at the blue edge of the spectral range. Thus, we decided to use the reduced spectra based on the IRAF analysis for 2016 Lick observations.

3. DATA ANALYSIS

3.1. Flux re-calibration

To reliably measure the spectral variability of the $H\beta$ line emission, we first perform flux re-calibration using the non-varying narrow [O III] line emission. This re-scaling approach described by van Groningen & Wanders (1992) is often adopted by various reverberation-mapping studies since the non-intrinsic variation caused by slightly inconsistent spectral resolution and slit loss due to the nightly change of the focus, seeing, and centering of AGN in the slit, etc (e.g., Peterson et al. 1995).

⁷ <https://mthamilton.ucolick.org/techdocs/instruments/kast/>

We utilize the python package `mapspec`⁸ (Fausnaugh 2017), which follows the same approach proposed by van Groningen & Wanders (1992), but works in a Bayesian framework, enabling assessment of the uncertainties of the calibration. As `mapspec` subtracts a linear continuum to extract the [O III] line flux within a user-defined window, we first transfer each spectrum into the rest-frame in order to use essentially the same [O III] extraction window for all objects. The extraction window of [O III] is defined as [4968, 5055]Å and the two adjacent continuum windows are selected to be [4963, 4968] and [5055, 5060]Å. After extracting [O III] of each epoch, `mapspec` matches the [O III] line profile of each epoch with that of the reference epoch using three parameters: a wavelength shift factor, a flux scaling factor, and a line broadening factor (i.e., the width of a Gauss-Hermite broadening kernel (Fausnaugh 2017)). We test various choices of the [O III] window and the broadening kernel, finding that the results are essentially the same.

As a reference epoch, we choose the broadest [O III] profile with S/N > 20 and degrade the [O III] line profiles of the other epochs to align them with the reference. The selected reference epoch is typically one of the epochs with bad seeing conditions and suffers from slit loss of the flux. One of the advantages of `mapspec` is that the uncertainty of each parameter can be estimated using the half amplitude of the 16th-84th quadrature interval of the distribution of MCMC samples. For each individual epoch, the derived uncertainty of the multiplicative factor is added in quadrature to the H β flux uncertainty. Thus, the epochs with more uncertain [O III]-based flux calibration have larger uncertainties in the H β light curves.

We further calibrate the absolute flux level of the spectroscopy by matching the synthetic *V*-band light curves with the photometric *V*-band light curves (or *R*-band for two objects, J1105+671 and PG 2251+113 at $z > 0.3$) using `PyCALI`. In this process we obtain an average scale factor and rescale the H β light curve for each object. The synthetic *V*(*R*)-band flux is calculated by performing synthetic photometry on the `mapspec`-calibrated spectra.

To verify the quality of the flux calibration, we calculate the normalized excess variance σ_{nx}^2 of the [O III] line flux (Barth et al. 2015) using the calibrated spectra of each target:

$$\sigma_{\text{nx}}^2 = \frac{1}{N\langle F \rangle^2} \sum_{i=1}^N [(F_i - \langle F \rangle)^2 - \delta_i^2], \quad (2)$$

⁸ <https://github.com/mmfausnaugh/mapspec/>

where N is the number of spectra, F_i and δ_i is the [O III] flux and flux uncertainty of epoch i , and $\langle F \rangle$ is the average of the [O III] flux. The normalized excess variance is the fractional residual scatter of the [O III] line flux, representing the systematic uncertainty of the flux calibration. While several previous studies uniformly added a single value of σ_{nx}^2 to each epoch's flux uncertainty in quadrature (e.g., Barth et al. 2015; U et al. 2022), we add the uncertainty of the [O III] scaling factor derived by `mapspec` to [O III] flux uncertainty in quadrature for each epoch. For completeness, we present σ_{nx} of each target in Table 2 to demonstrate the quality of the flux scaling.

We note that for AGNs with a weak [O III] line, this procedure introduces a large systematic error since it is difficult to define the [O III] line profile because of the blending of strong Fe II and [O III] lines. In our sample, five objects, namely, J0939+375, PG 1121+422, PG 1322+659, PG 1440+356, and J1526+275, show a relatively small [O III] equivalent width. As a different approach, we obtain a flux scale factor for each epoch by matching the synthetic *V* band magnitude with the *V* band magnitude from the interpolated photometry light curve based on the DRW model provided by `PyCALI`. By comparing the results from two different calibration approaches, we find that only one target J1526+275 with the weakest (almost no narrow) [O III] line shows noticeably better cross-correlation results from the photometry-based scaling. Therefore, we adopt the photometry-based scaling result for J1526+275, while we use the [O III]-based scaling results for the rest of the targets.

3.2. Mean and rms spectra

We generate the mean and rms spectra using the flux re-calibrated spectra of each target, as done by previous studies (e.g., Peterson et al. 2004; Barth et al. 2015; Rakshit et al. 2019). The mean spectra are calculated by averaging the flux of all epochs, while the rms spectra are generated using the definition:

$$S_\lambda = \left(\frac{1}{N-1} \sum_{i=1}^N (f_{\lambda,i} - \bar{f}_\lambda)^2 \right)^{1/2}, \quad (3)$$

where N is the number of spectra, $f_{\lambda,i}$ and \bar{f}_λ is the flux density of the spectrum from the i th epoch and the mean spectrum, respectively.

We provide two sets of rms spectra, using the individual epoch's spectra with and without subtracting continuum and narrow emission lines (see §3.3 for the decomposition process). It has been shown that the rms spectra generated without subtracting continuum and

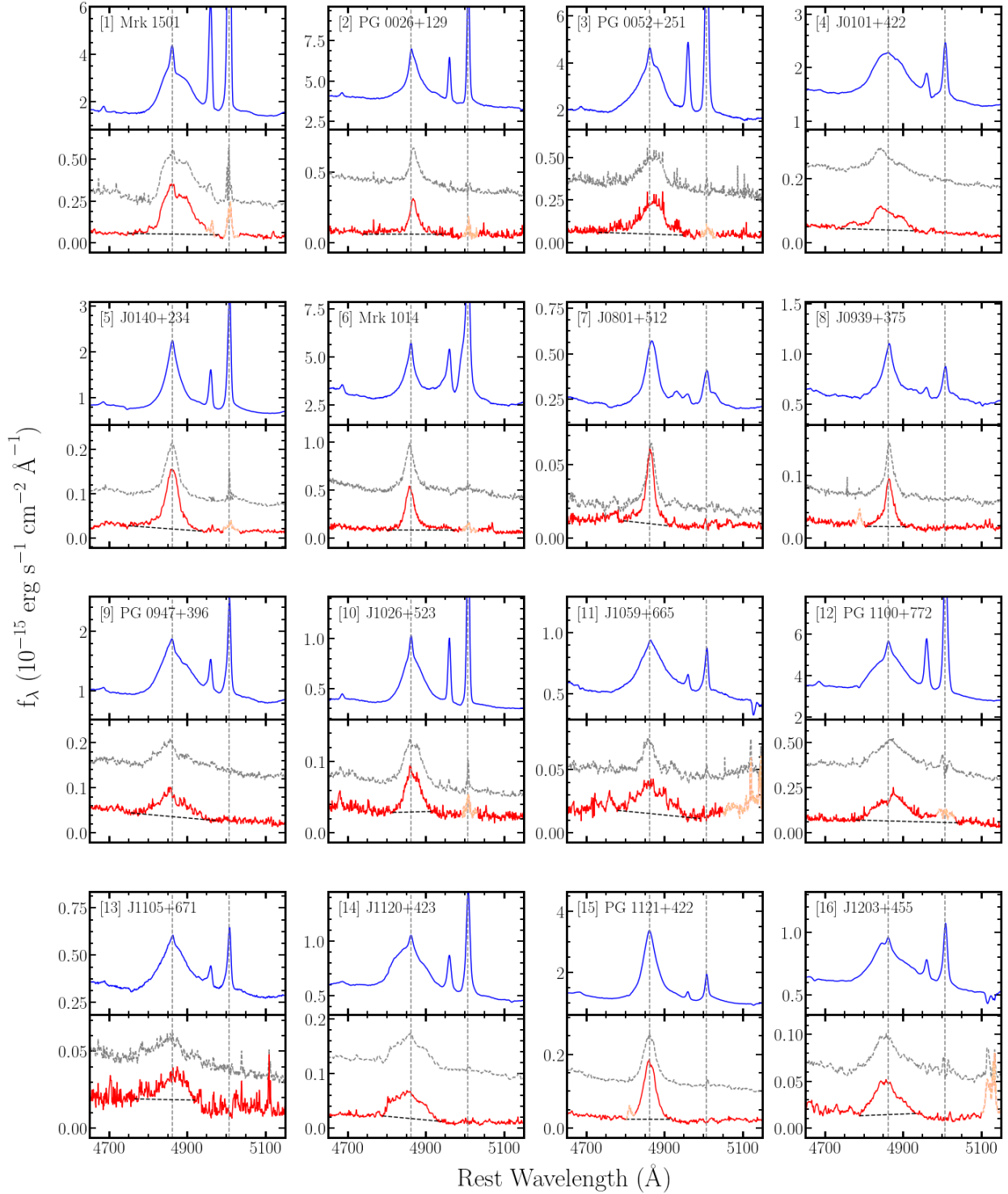


Figure 2. The H β emission line profiles in the mean (upper panel) and rms spectra (lower panel) of each AGN. The red and grey lines represent the rms spectra, calculated from the individual spectra with and without subtracting continuum and narrow lines, respectively. The two vertical dashed lines indicate the peak of H β and [O III] λ 5007. Some features caused by skylines or [O III] residuals are masked (orange dashed lines).

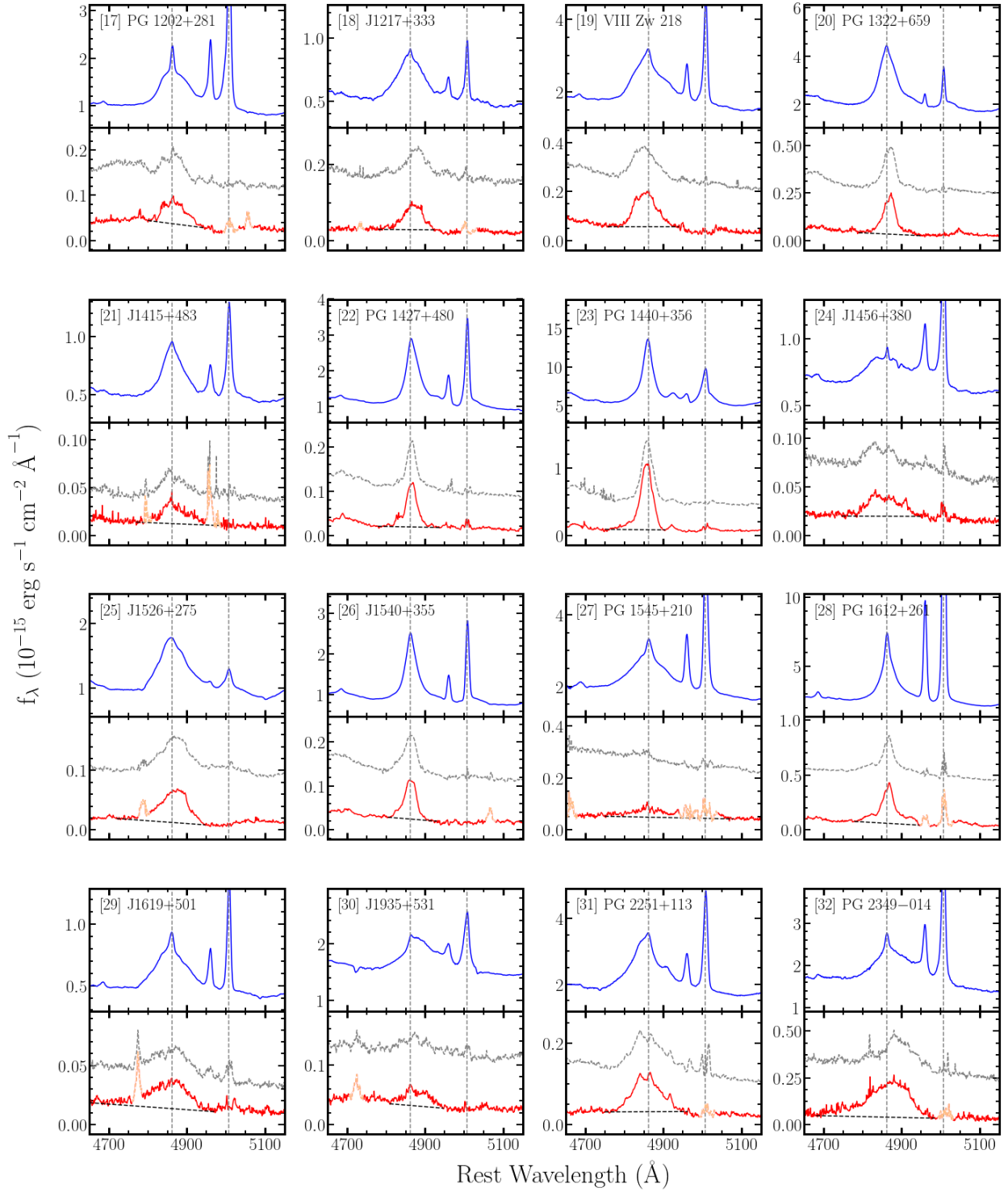


Figure 2. Continued.

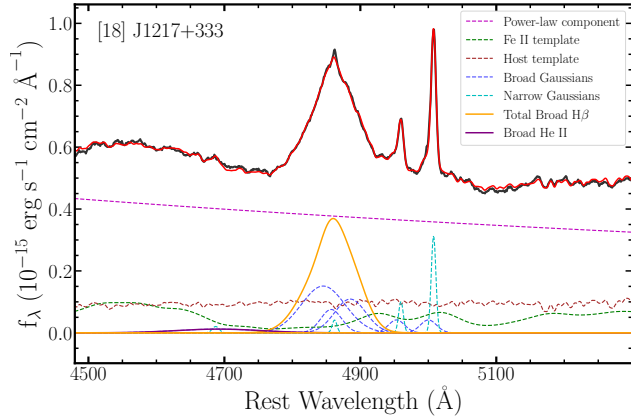


Figure 3. Decomposition of mean spectrum for J1217+333 as an example. The black and red solid lines represent the mean spectrum and best-fit model. The continuum model consists of a power-law (magenta dashed) component, a Fe II template (green dashed), and a host galaxy template (brown dashed). Broad and narrow Gaussians are displayed using blue and cyan dashed lines, while the total broad H β and He II profiles are shown by orange and purple solid lines.

narrow lines can suffer from a bias in the line width measurement because of the different variations between the continuum and emission line fluxes (Barth et al. 2015; Wang et al. 2019). As presented in Figure 2, we find a small residual at the location of [O III] λ 5007, indicating the high quality of the flux calibration. The noticeable residual of [O III] in the rms spectra of some targets, together with other small features caused by the telluric lines or the CCD cosmetics and cosmic rays are masked out (as indicated by orange color in Figure 2) and interpolated before the line width calculation. Note that because we have different wavelength coverages owing to three instrumental setups of Lick spectroscopy, there are small rises of the continuum at the blue side of H β (e.g., PG 1440+356 and Mrk 1501) due to the CCD effect.

3.3. Spectral decomposition and measurements

We perform spectral decomposition on the mean spectrum to remove the host contamination, if any, and measure the line flux and width of the broad H β . The same procedure is adopted to fit the spectrum of each epoch to derive the light curve of the H β line flux. Compared to the linear fit of the continuum under the H β line profile, the spectral decomposition approach can better isolate the blended components, e.g., H β and Fe II. Thus, the decomposition approach has been adopted in a number of recent studies, particularly based on high-quality spectra (e.g., Park et al. 2012b; Barth et al. 2015; Hu et al. 2015, 2021; U et al. 2022).

We adopt the spectral decomposition procedure of the previous studies by Shen et al. (2011, 2019) with slight

modifications. Here, we summarize the basics of the fitting procedure. First, we generated a pseudo-continuum model by combining a power law, an Fe II component, and a host galaxy stellar population model, in order to fit the observed spectra within two line-free windows, i.e., [4450,4600] and [5050, 5550] \AA in the rest-frame. We apply velocity shift and Gaussian velocity broadening to the iron and host templates, respectively. For the Fe II model, we test two commonly used templates provided by Boroson & Green (1992) and Kovačević et al. (2010). In the case of the template of Kovačević et al. (2010), it is difficult to use consistent flux ratios of different emission line groups for individual epochs, because of the variation of the wavelength coverage due to the different spectroscopy setups of the MDM and Lick observations. Thus, we decide to use the Fe II template of Boroson & Green (1992). However, we find that the Fe II template of Kovačević et al. (2010) provides a more accurate fit for several objects (e.g., Mrk 1501 and Mrk 1014, see Barth et al. 2015; U et al. 2022). Thus, we adopt the fits using Kovačević et al. (2010) iron template for these objects. In the case of the host galaxy stellar population model, we used a single-burst 10 Gyr old stellar population model with solar metallicity (Bruzual & Charlot 2003). As our targets are moderate to high luminosity AGNs, the host galaxy stellar absorption line features are negligible in the mean spectra of most targets. We present one example of the spectral decomposition using the lowest luminosity AGN, J1217+333, in our sample in Figure 3. As expected from its low AGN luminosity, the host component, i.e., the strong of Mg Ib $\lambda\lambda$ 5167,5173,5184 triplet absorption, is clearly detected. In contrast, most of the other objects show no clear sign of host galaxy absorption lines in their mean spectrum.

After subtracting the best-fit pseudo continuum model, we fit the residual emission lines with Gaussian models by accounting for various kinematical features of individual emission lines. Specifically, we use three Gaussians for the broad H β line and one Gaussian for the narrow H β component. For [O III] λ 4959 and [O III] λ 5007, we use two Gaussian models for the central and wing components. In addition, one narrow and one broad Gaussian models were used for fitting the narrow and broad components of He II λ 4687. All the narrow line centers and widths are tied together.

3.4. H β Light Curves

We measure the H β line flux based on the decomposition and generated the light curves over the 6-year monitoring period. Note that we apply a window to each epoch’s spectrum, within which the H β line flux was summed, as listed in Table 3. These additional win-

Table 2. Light curve statistics

Name (1)	MJD range (2)	Continuum light curve				H β light curve				
		Band (3)	N _{obs} (4)	$\overline{\Delta(T)}$ (5)	F_{var} (6)	N _{obs} (7)	$\overline{\Delta(T)}$ (8)	F_{var} (9)	σ_{nx} (10)	
1	Mrk 1501	57689-59430	<i>B + g</i>	375	1	0.20±0.01	38	15	0.17±0.02	0.002
2	PG 0026+129	57689-59395	<i>B + g</i>	381	1	0.10±0.00	30	19	0.06±0.01	0.003
3	PG 0052+251	57689-59391	<i>B + g</i>	378	2	0.20±0.01	37	16	0.09±0.01	0.002
4	J0101+422	57327-59430	<i>B</i>	256	4	0.15±0.01	84	13	0.10±0.01	0.006
5	J0140+234	57327-59391	<i>B</i>	232	4	0.15±0.01	87	14	0.10±0.01	0.002
6	Mrk 1014	57689-59261	<i>B + g</i>	330	2	0.14±0.01	31	20	0.20±0.03	0.006
7	J0801+512	57327-59342	<i>B</i>	213	6	0.15±0.01	31	25	0.11±0.01	0.005
8	J0939+375	57327-59377	<i>B</i>	241	5	0.16±0.01	57	16	0.12±0.01	0.008
9	PG 0947+396	57327-59377	<i>B</i>	268	4	0.15±0.01	72	14	0.08±0.01	0.004
10	J1026+523	57327-59386	<i>B</i>	272	5	0.21±0.01	73	15	0.14±0.01	0.003
11	J1059+665	57359-59377	<i>B</i>	214	6	0.10±0.01	36	28	0.08±0.01	0.011
12	PG 1100+772	57327-59386	<i>B</i>	241	5	0.08±0.00	40	28	0.11±0.01	0.002
13	J1105+671	57351-59366	<i>V</i>	204	6	0.17±0.01	29	29	0.13±0.02	0.009
14	J1120+423	57328-59387	<i>B</i>	260	4	0.18±0.01	48	16	0.11±0.01	0.003
15	PG 1121+422	57328-59402	<i>B</i>	234	4	0.13±0.01	61	17	0.05±0.01	0.004
16	J1203+455	57345-59386	<i>B</i>	232	4	0.12±0.01	49	18	0.11±0.01	0.005
17	PG 1202+281	57345-59402	<i>B</i>	250	4	0.16±0.01	84	14	0.08±0.01	0.002
18	J1217+333	57334-59386	<i>B</i>	247	4	0.20±0.01	60	15	0.14±0.02	0.014
19	VIII Zw 218	57346-59402	<i>B</i>	240	4	0.15±0.01	79	14	0.11±0.01	0.003
20	PG 1322+659	57361-59404	<i>B</i>	249	4	0.14±0.01	65	17	0.06±0.01	0.022
21	J1415+483	57384-59358	<i>B</i>	203	5	0.11±0.01	30	21	0.07±0.01	0.003
22	PG 1427+480	57388-59395	<i>B</i>	227	5	0.11±0.01	57	14	0.05±0.01	0.001
23	PG 1440+356	57389-59404	<i>B</i>	236	4	0.11±0.01	62	15	0.12±0.01	0.002
24	J1456+380	57384-59404	<i>B</i>	271	4	0.12±0.01	79	15	0.12±0.01	0.004
25	J1526+275	57384-59404	<i>B</i>	237	5	0.10±0.01	51	18	0.05±0.01	0.006
26	J1540+355	57385-59404	<i>B</i>	237	4	0.15±0.01	81	16	0.06±0.01	0.003
27	PG 1545+210	57385-59431	<i>B</i>	239	4	0.14±0.01	69	18	0.06±0.01	0.001
28	PG 1612+261	57389-59431	<i>B</i>	210	4	0.19±0.01	32	17	0.10±0.01	0.001
29	J1619+501	57385-59431	<i>B</i>	277	4	0.11±0.01	84	15	0.08±0.01	0.004
30	J1935+531	57333-59430	<i>B + g</i>	778	1	0.07±0.00	81	14	0.07±0.01	0.006
31	PG 2251+113	57711-59404	<i>V + g</i>	295	2	0.07±0.00	28	17	0.06±0.01	0.002
32	PG 2349-014	57689-59392	<i>B + g</i>	233	3	0.18±0.01	34	16	0.18±0.02	0.005

Notes. Column (1): object name. Column (2): monitoring time baseline in MJD. Column (3): Continuum band. Column (4): number of epochs in photometry. Column (5): Median cadence in days. Column (6): Noise-corrected fractional variability F_{var} and its uncertainty as defined in equation 4 and 5. Column (7): number of epochs in spectroscopy. Column (8): Median cadence in days. Column (9): Noise-corrected fractional variability F_{var} and its uncertainty. Column (10): normalized excess standard deviation of [O III] flux after spectral calibration by `mapspec` (see §3.1).

dows are added to avoid any over-fitting to the noise at the edge of the line profile.

Note that while both Lick and MDM spectra were aligned to the same reference spectrum during the flux re-calibration process using the non-varying [O III] emission line, there still can be a small offset between two sets of the light curves from two different telescopes, Lick and MDM, due to slightly different aperture effects (Peter-

son et al. 1995). We further match the two light curves from Lick and MDM telescopes by assuming the spectra obtained at similar time should have the same flux level. By searching for pairs of close epochs within one day between the Lick and MDM observations, we calculated the median scaling ratio between the two spectra using these pairs. Finally, the MDM light curves are

Table 3. H β line flux extraction window and average flux

(1)	(2)	(3)	
Name	Window	$\overline{F_{H\beta}}$	
1	Mrk 1501	4810-4929	156±26
2	PG 0026+129	4783-4941	168±11
3	PG 0052+251	4790-4935	186±17
4	J0101+422	4778-4945	94±11
5	J0140+234	4810-4915	67±7
6	Mrk 1014	4806-4918	103±21
7	J0801+512	4814-4910	16±2
8	J0939+375	4808-4916	23±3
9	PG 0947+396	4787-4946	74±6
10	J1026+523	4799-4925	34±5
11	J1059+665	4790-4934	37±3
12	PG 1100+772	4779-5050	159±18
13	J1105+671	4790-4935	25±3
14	J1120+423	4779-4945	45±5
15	PG 1121+422	4810-4914	108±7
16	J1203+455	4769-4956	32±4
17	PG 1202+281	4779-4945	76±7
18	J1217+333	4795-4930	34±6
19	VIII Zw 218	4778-4946	122±14
20	PG 1322+659	4811-4913	129±9
21	J1415+483	4805-4919	29±2
22	PG 1427+480	4812-4912	79±4
23	PG 1440+356	4821-4903	238±29
24	J1456+380	4764-4960	27±3
25	J1526+275	4796-4928	55±4
26	J1540+355	4814-4911	65±5
27	PG 1545+210	4769-4996	132±8
28	PG 1612+261	4795-4929	197±21
29	J1619+501	4783-4941	37±3
30	J1935+531	4775-4920	51±4
31	PG 2251+113	4772-4952	205±14
32	PG 2349-014	4748-4994	102±18

Notes. Column (1): object name. Column (2): Extraction window for the line flux measurements in the rest-frame in the unit of Å. Column (3): average flux ($\overline{F_{H\beta}}$) of H β light curves as well as its standard deviation in the unit of 10^{-15} erg s $^{-1}$ cm $^{-2}$.

scaled with these ratios to match with the Lick light curves.

For each object, we calculate the noise-corrected fractional variability F_{var} of both continuum and H β light curves as this quantity is frequently adopted to represent the level of variability (e.g., Peterson et al. 2004; Bentz et al. 2009b). The F_{var} and its uncertainty is defined by (Rodríguez-Pascual et al. 1997; Edelson et al. 2002) as:

$$F_{\text{var}} = \frac{1}{\langle f \rangle} \sqrt{\sigma^2 - \delta^2} \quad (4)$$

$$\sigma_{F_{\text{var}}} = \frac{1}{\sqrt{2N}F_{\text{var}}} \frac{\sigma^2}{f^2}, \quad (5)$$

where N is the number of epochs, the $\langle f \rangle$ and σ are the mean flux and standard deviation of the light curve, and the δ is the rms of individual flux uncertainties. We list the F_{var} of continuum and H β in Table 2. For our sample, F_{var} of continuum ranges from 0.07 to 0.21, while the F_{var} of H β ranges from 0.05 to 0.20. Note that 30 out of 32 objects in the sample show continuum $F_{\text{var}} \geq 0.1$, indicating clear detection of the variability of the majority of the targets.

Table 4. B band and H β light curves

Name	Band	Telescope	MJD	F	F_{err}
Mrk 1501	B	MDM13	57689.6641	1.694	0.049
Mrk 1501	B	MDM13	57690.6992	1.612	0.049
Mrk 1501	B	MDM13	57697.6797	1.675	0.051
Mrk 1501	B	MDM13	57698.6914	1.772	0.056
Mrk 1501	B	MDM13	57699.6133	1.660	0.059
Mrk 1501	B	MDM24	57710.7148	1.734	0.069
Mrk 1501	B	MDM13	57711.6953	1.802	0.049
Mrk 1501	B	MDM13	57712.7617	1.839	0.051

Notes. For B band light curves the quantity F represent the flux density in the unit of 10^{-15} erg s $^{-1}$ cm $^{-2}$ Å $^{-1}$, while for H β (Band=H β) the quantity F represent the integrated H β flux in the unit of 10^{-15} erg s $^{-1}$ cm $^{-2}$. This table is available in its entirety online.

4. RESULTS

4.1. H β lag measurement

The emission line lags have been measured in a number of different ways in the previous RM studies. These methods are categorized into two main classes: the traditional cross-correlation analysis and the methods with statistical approach for describing AGN variability, e.g., damped random walk (DRW) models (e.g., Kelly et al. 2009; MacLeod et al. 2010). The former class includes the interpolated cross-correlation function (ICCF, e.g., Gaskell & Peterson 1987; Peterson et al. 1998), the discrete correlation function (DCF, Edelson & Krolik 1988), and the z-transformed discrete correlation function (zDCF, Alexander 2013), while the second class includes JAVELIN (Zu et al. 2011), CREAM (Starkey et al. 2016), and MICA (Li et al. 2016). It has been demonstrated that for sparsely sampling light curves, DCF and zDCF are less efficient in recovering the lag than ICCF and JAVELIN (White & Peterson 1994; Li et al. 2019). While comprehensive comparison among the second-class methods is not yet available, these methods generally share a similar basic algorithm and at least

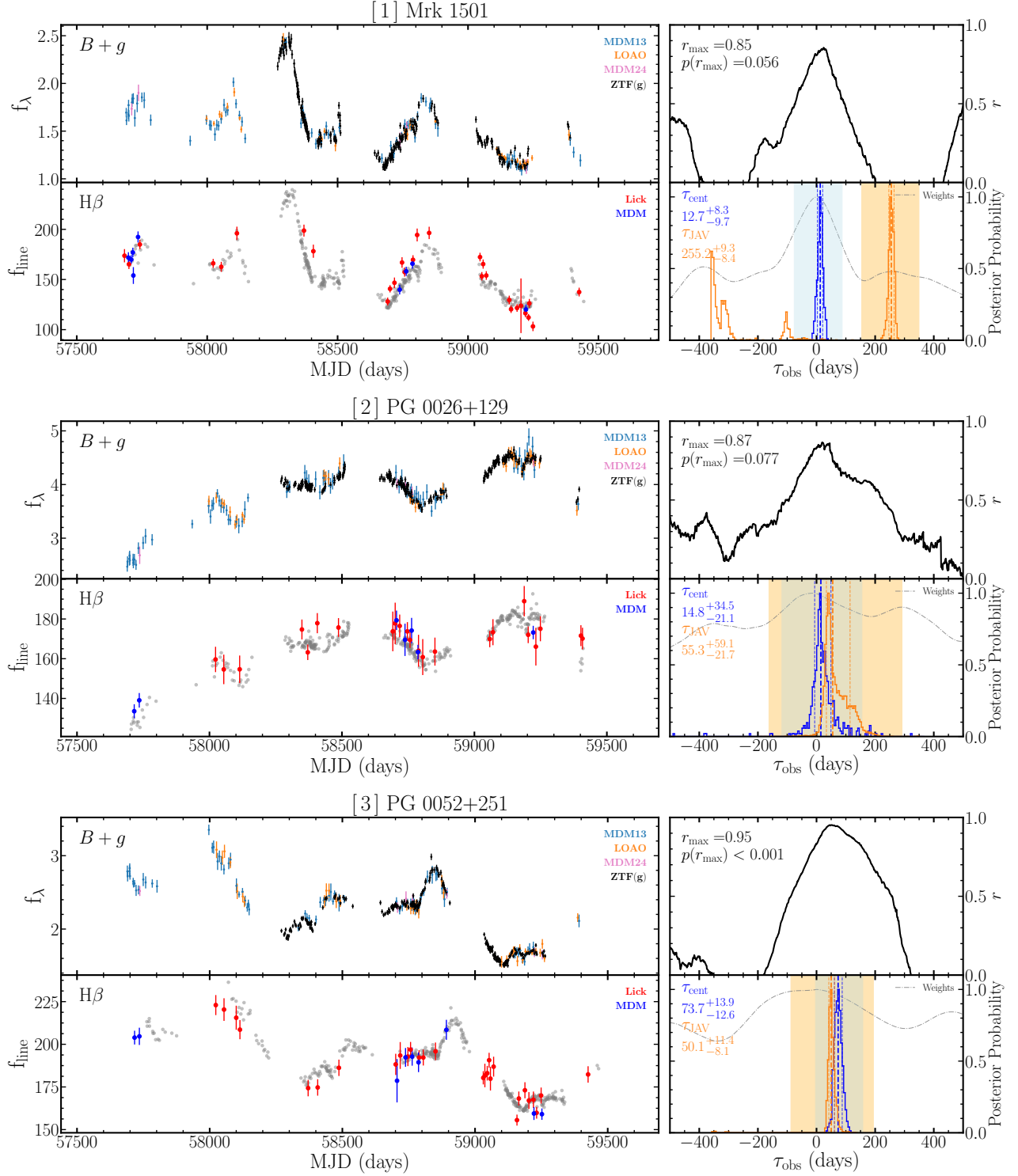


Figure 4. Light curves of the continuum (upper left) and H β (lower left) in units of $10^{-15} \text{ erg s}^{-1} \text{ cm}^{-2} \text{ \AA}^{-1}$ and $10^{-15} \text{ erg s}^{-1} \text{ cm}^{-2}$, respectively, along with the ICCF (upper right) and the posterior distribution in the observed-frame (lower right) for each AGN. The unweighted posterior probability distribution of ICCF τ_{cent} (blue) and JAVELIN τ_{JAV} (orange) as well as the applied weight (dotted-dashed line) for searching the primary peak (see §4.1) are presented in the lower right panel. The blue and orange shadowed areas indicate the range of the primary peak for τ_{cent} and τ_{JAV} , respectively. The vertical solid and dashed lines represent the location of the lag and its upper and lower limit calculated as the median, 16th, and 84th percentile within the primary peak range, respectively. τ_{cent} is adopted as the final lag measurement, by which the continuum light curve is shifted and matched with the H β light curves as visualized by grey points in the lower left panel. The two lag reliability indicators, i.e., the r_{max} and $p(r_{\text{max}})$ (see §4.3 for details), are displayed in the upper right panel.

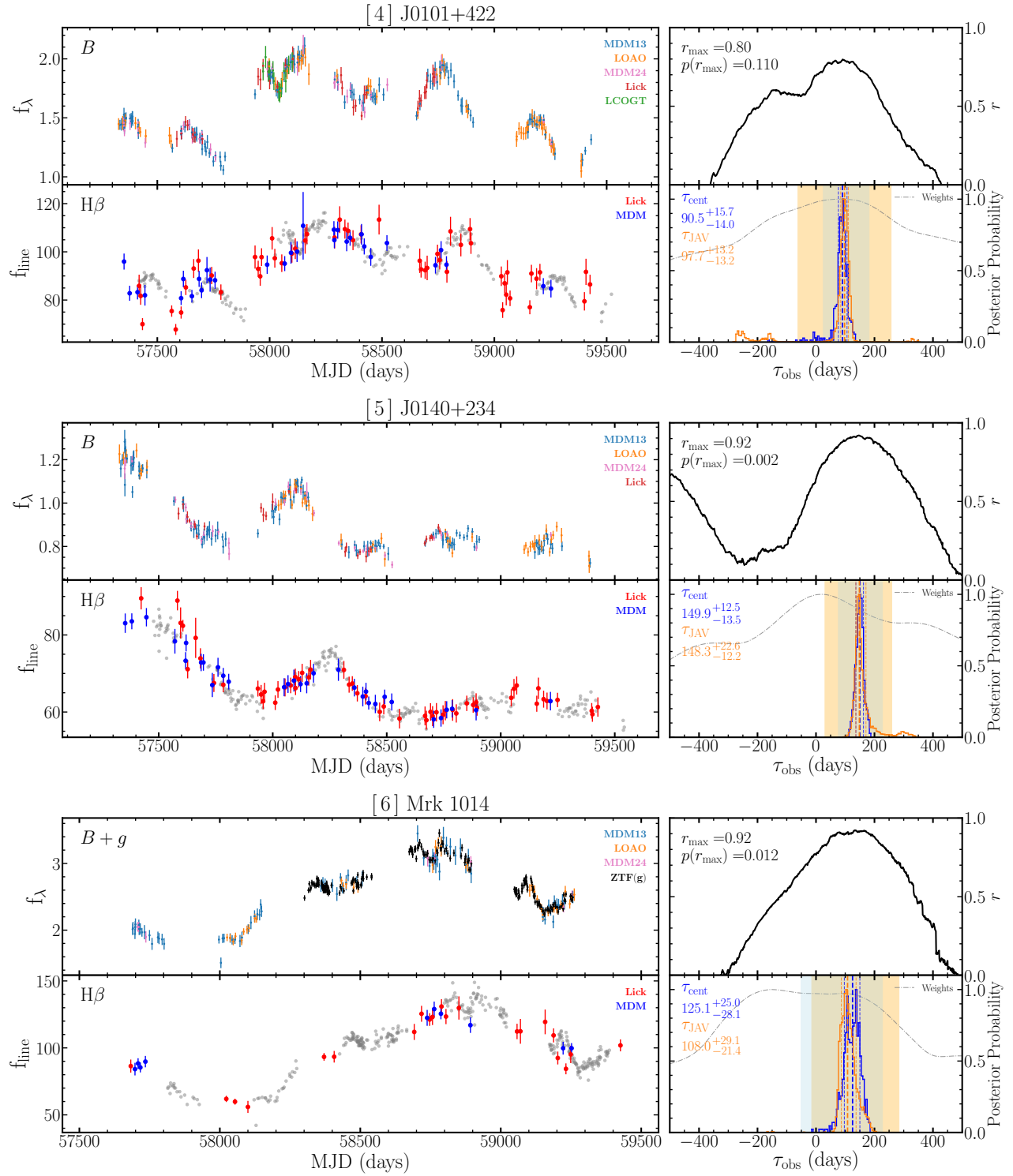


Figure 5. Same as Figure 4 but for J0101+422, Mrk 1014, and J0801+512.

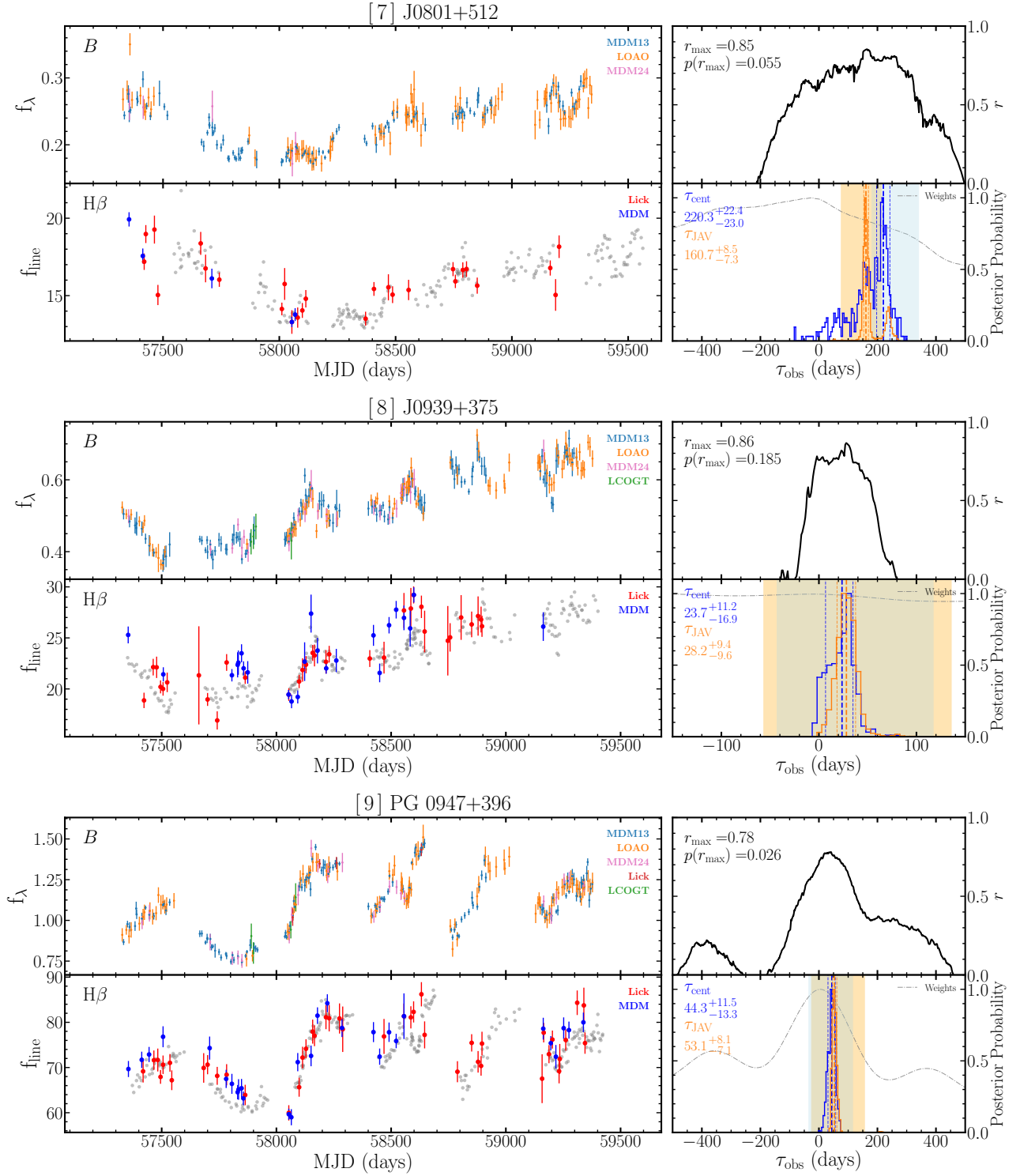


Figure 6. Same as Figure 4 but for J0801+512, J0939+375, and PG0947+396.

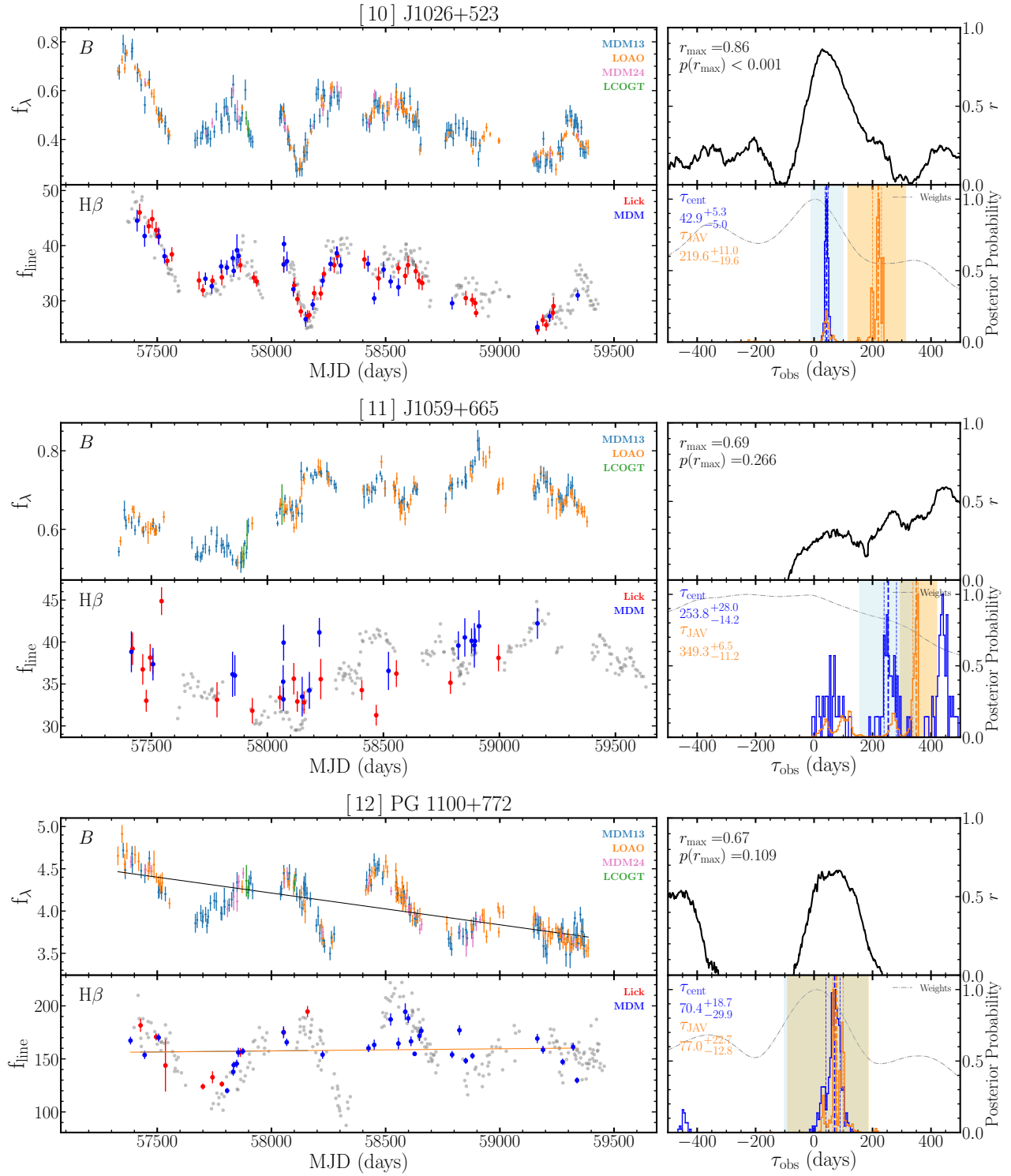


Figure 7. Same as Figure 4 but for J1026+523, J1059+665, and PG 1100+772.

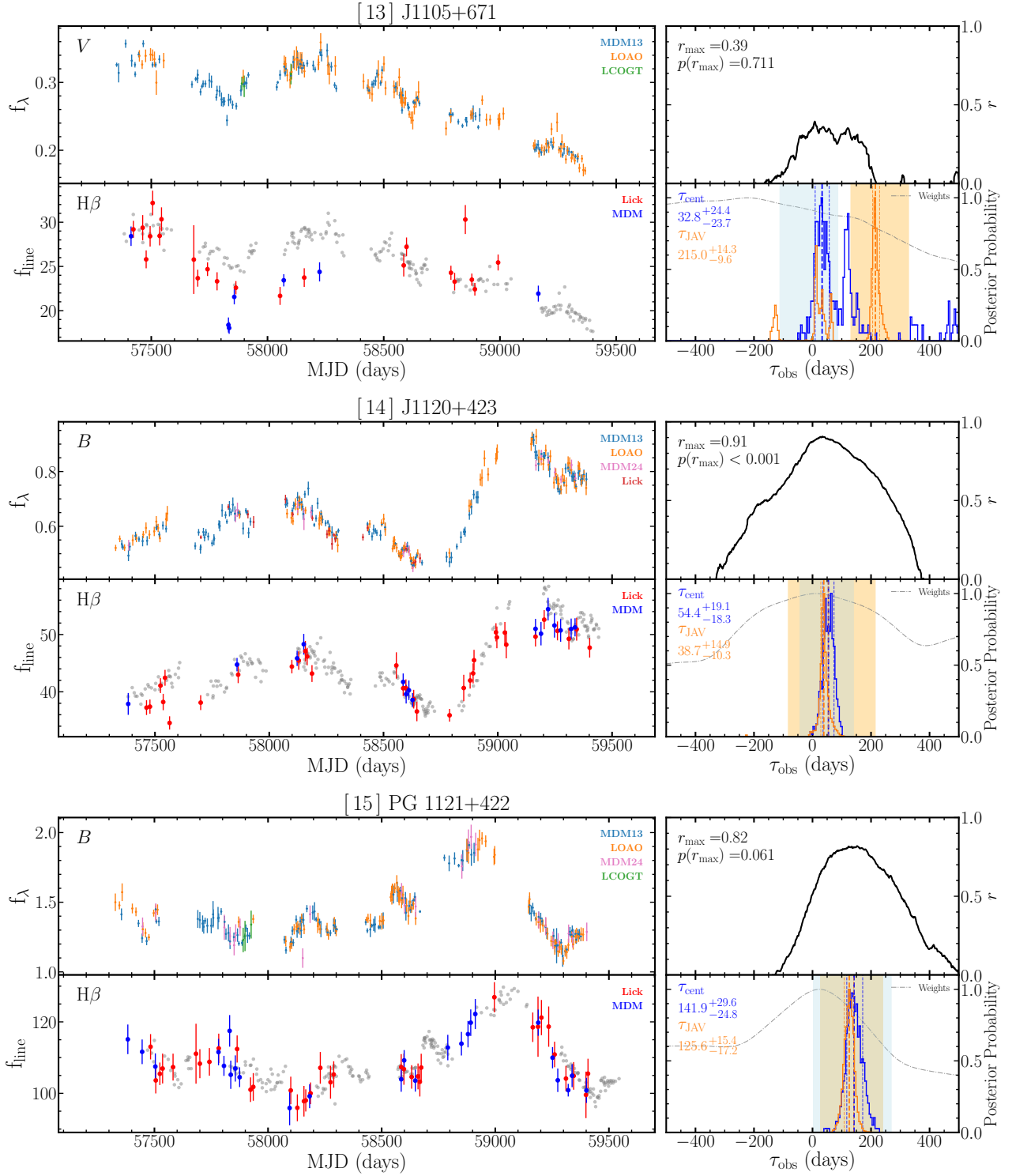


Figure 8. Same as Figure 4 but for J1105+671, J1120+423, and PG 1121+422.

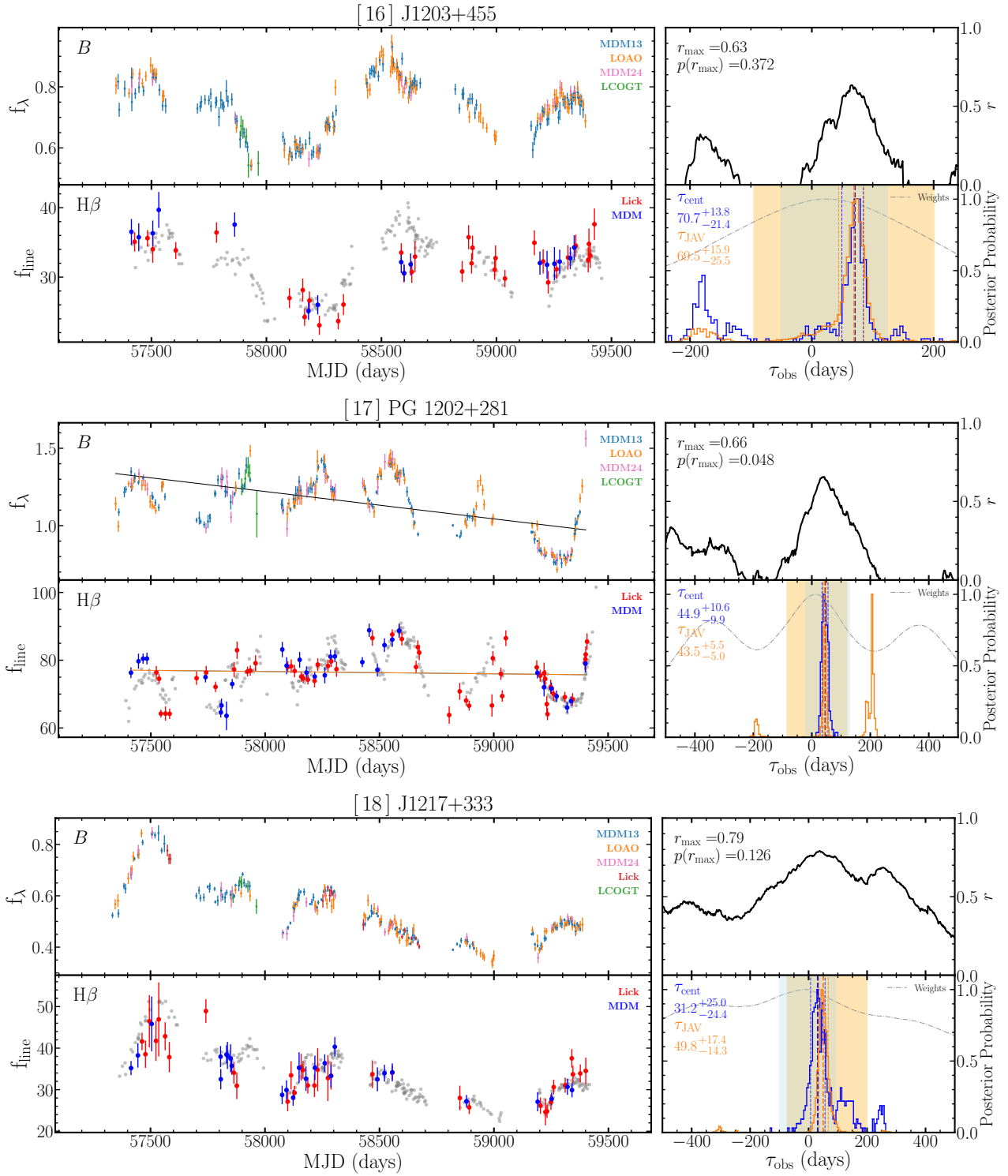


Figure 9. Same as Figure 4 but for J1203+455, PG 1202+281, and J1217+333.

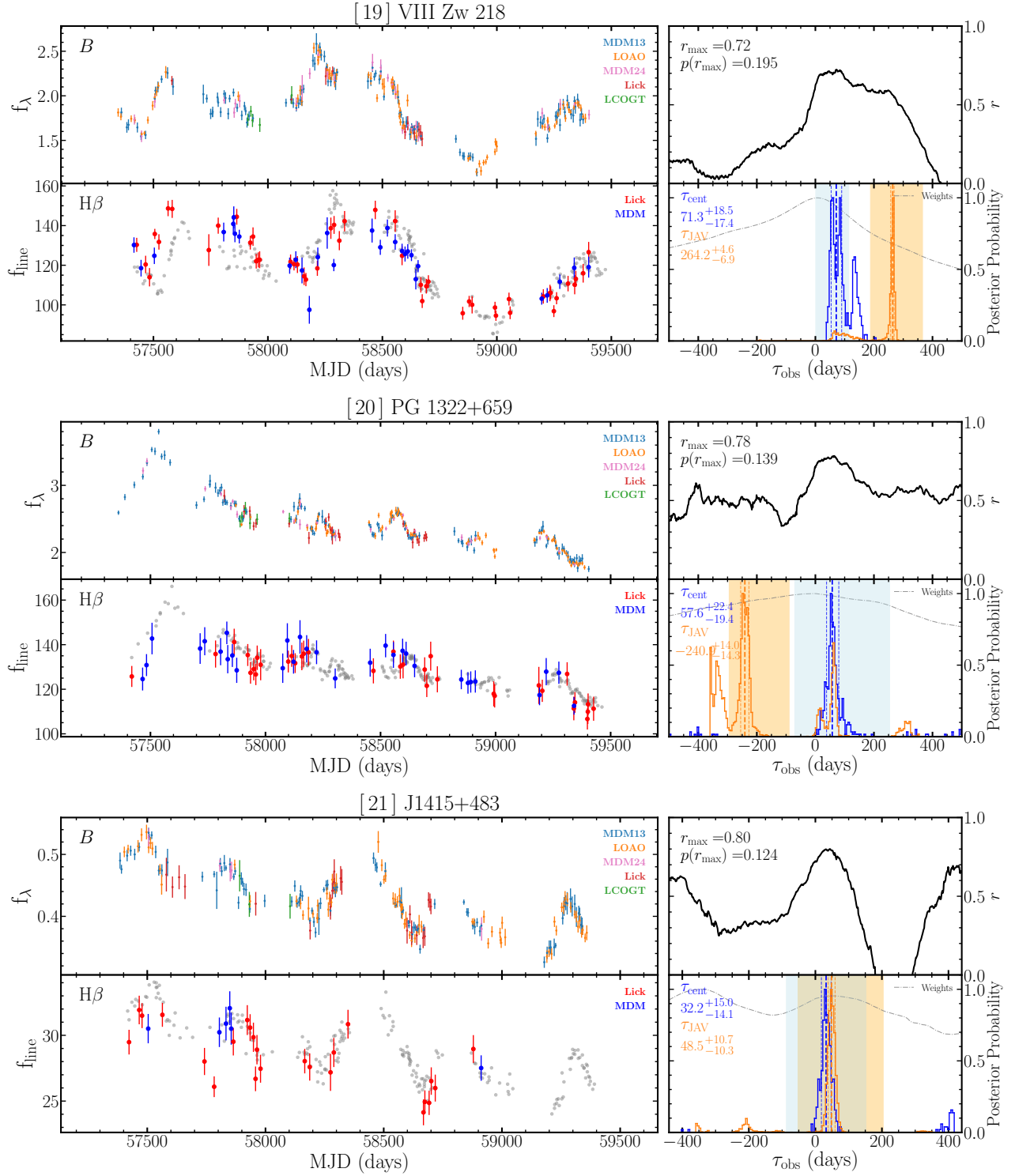


Figure 10. Same as Figure 4 but for VIII Zw218, PG 1322+659, and J1415+483.

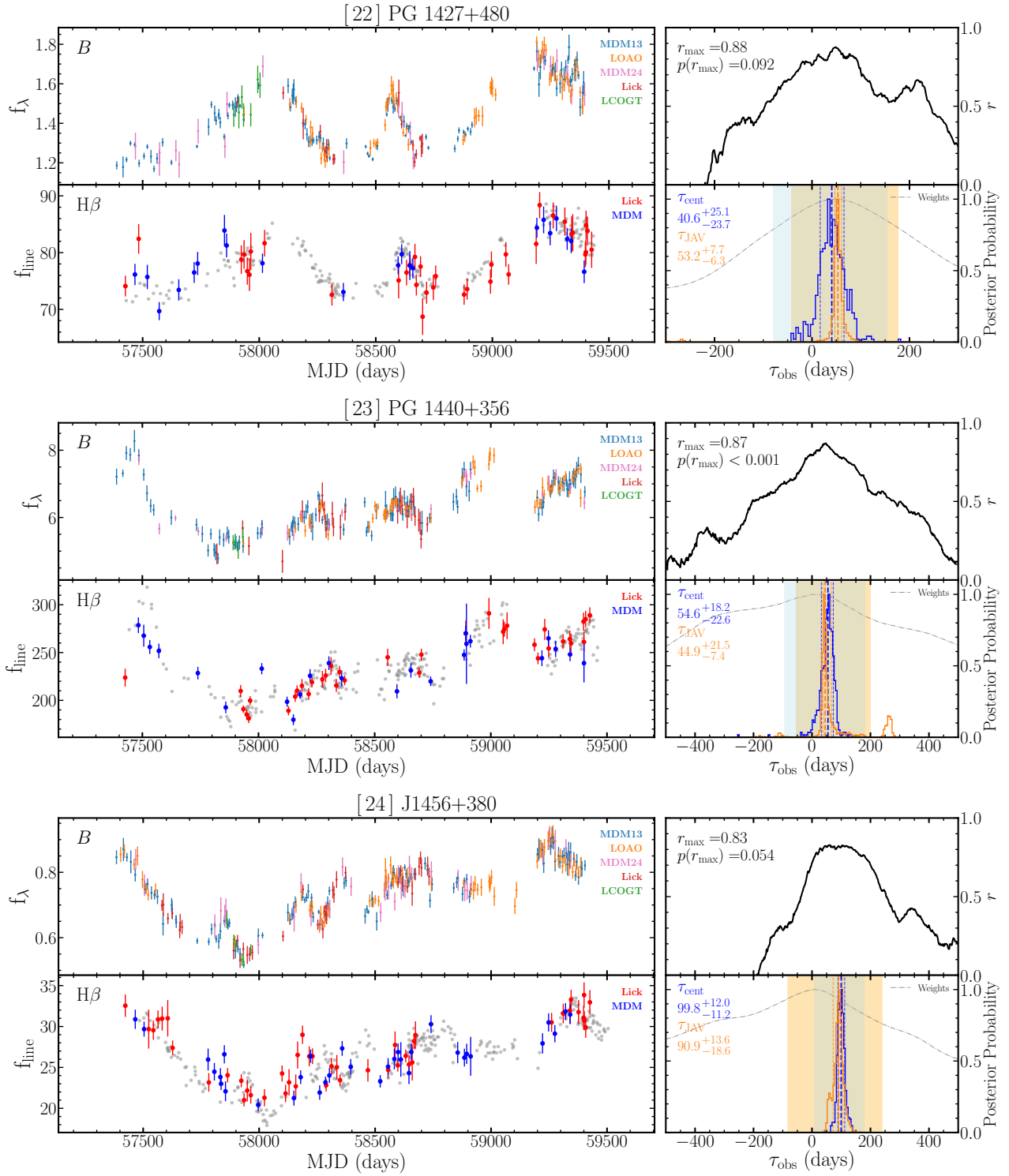


Figure 11. Same as Figure 4 but for PG 1427+480, PG 1440+356, and J1456+380.

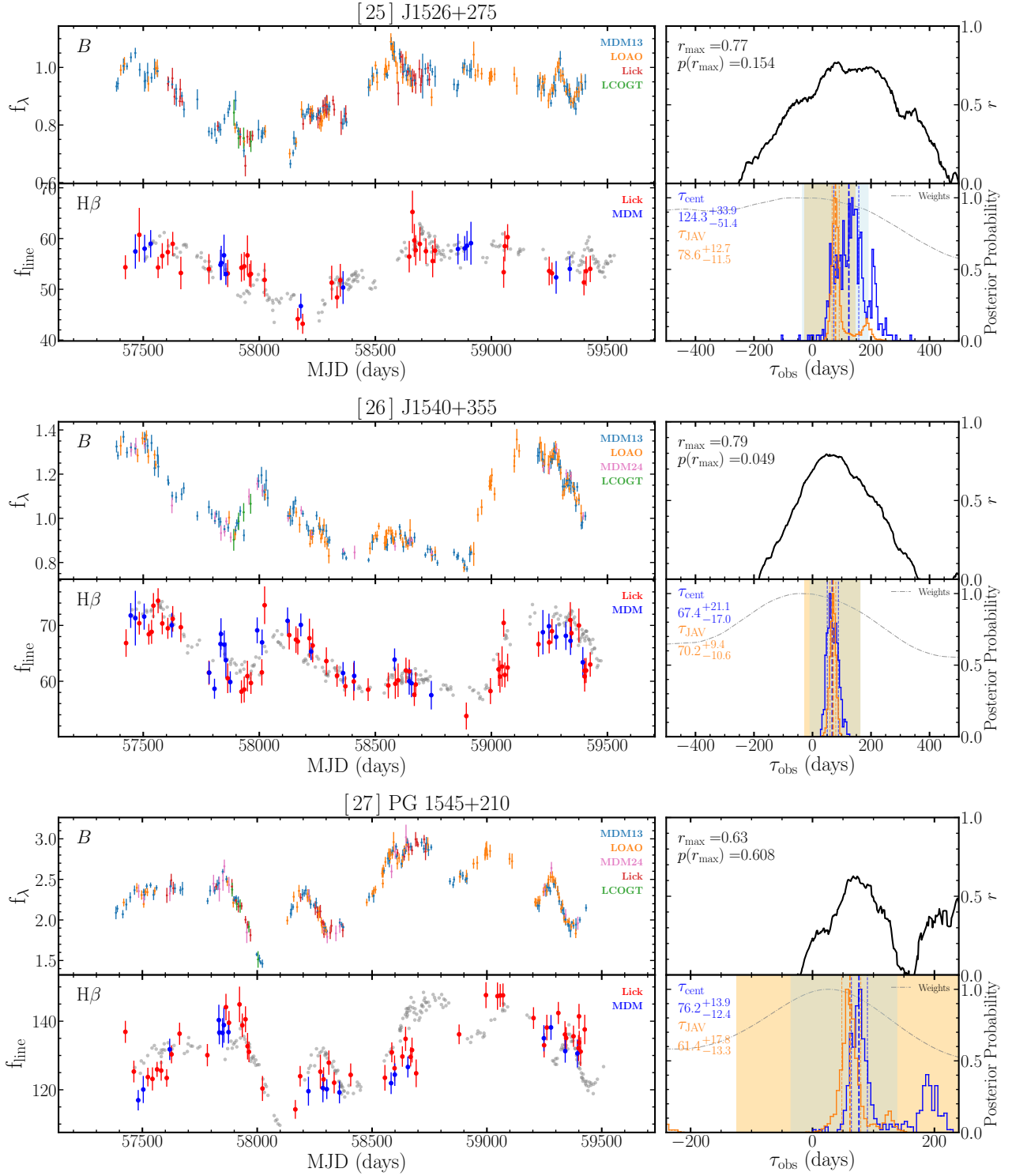


Figure 12. Same as Figure 4 but for J1526+275, J1540+355, and PG 1545+210.

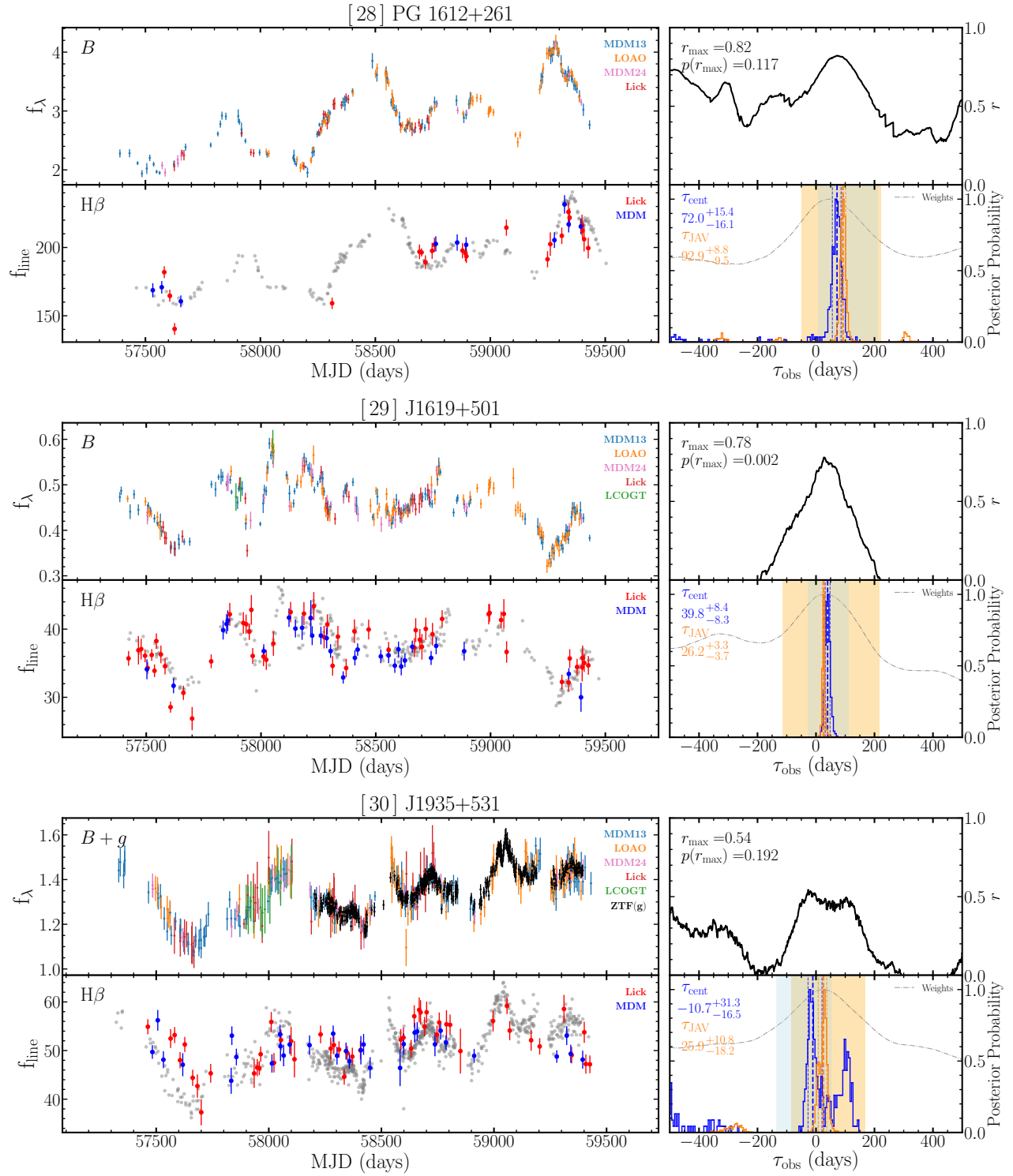


Figure 13. Same as Figure 4 but for PG 1612+261, J1619+501, and J1935+531.

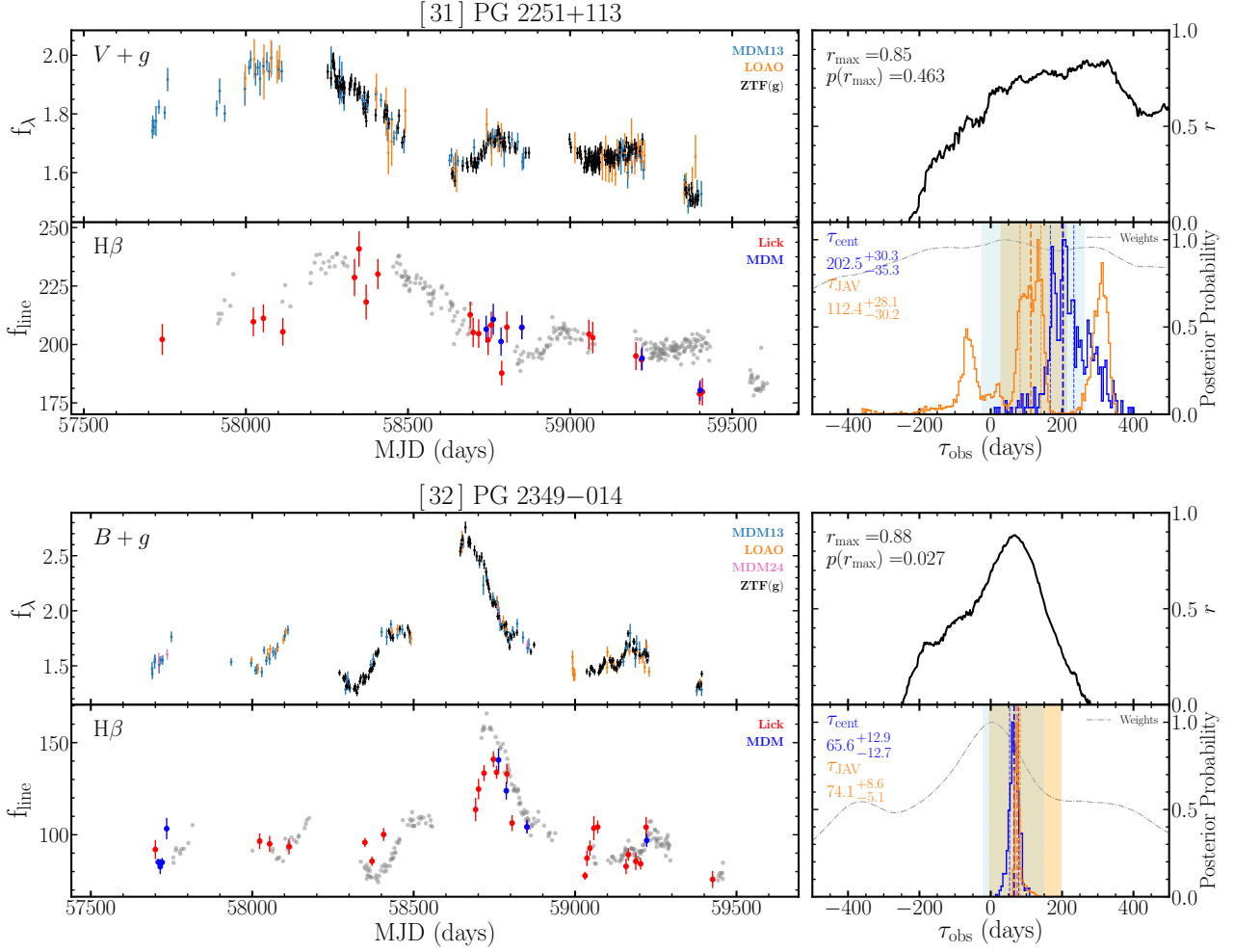


Figure 14. Same as Figure 4 but for PG 2251+113 and PG 2349–014.

some of them provide consistent results (e.g., Grier et al. 2017, 2019).

We adopt the most commonly used approach ICCF as the primary method for the lag measurements of SAMP targets. As the ICCF method has been adopted by the majority of previous studies, it is possible to directly compare with the previously reported measurements. We use the python package PyCCF (Peterson et al. 1998; Sun et al. 2018) to perform the lag measurements, by calculating the cross-correlation coefficient r between the continuum and H β emission line light curves after linearly interpolating one light curve to match the time grid of the other light curve. One light curve is shifted by a series of τ values in a searching window, and as a function of τ , ICCF is calculated and the cross-correlation coefficient r is determined. In this process, either the continuum or the emission-line light curve is interpolated to calculate the ICCF and the final ICCF is obtained by averaging the two ICCFs. Then, the centroid (τ_{cent}) or the peak (τ_{peak}) is determined us-

ing the range in the averaged ICCF, where r is larger than 80% of its maximum, and adopted as the lag of the two light curves. We consider τ_{cent} as the primary ICCF lag measurements as done by previous studies (e.g., Peterson et al. 2004), while we also present τ_{peak} of each AGN for comparison and completeness in Table 5. The lag uncertainties are estimated with the flux randomization/random subset sampling (FR/RSS) method, which randomizes the flux of each epoch based on its uncertainty and randomly selects a subset of epochs in the light curve for each simulation (Peterson et al. 1998).

In the ICCF analysis, we use a searching window of $[-600, 600]$ days with a step of 1 day. Note that this window is roughly 30% of our 6-year baseline (~ 2000 days on average) and at least a factor of 3 larger than the expected lag estimated based on the size-luminosity relation (Bentz et al. 2013). For two targets, PG 1100+772 and PG 2251+113, the searching window is less than a factor of 2 of their expected lags. Thus, we test the effect of the size of the searching window by increasing the

searching window as $[-1000, 1000]$ days, finding that the lags are essentially the same. For J1415+483, which is the only target that was monitored for 5 years, we use a searching window of $[-445, 445]$ days, corresponding to $\sim 30\%$ of its baseline. In the case of the JAVELIN analysis, we initially use the same searching window. However, we finally use a smaller searching window, $[-360, 360]$ days, because we find JAVELIN tends to provide strong aliases if we use a larger searching window, and sometimes unacceptably large lag values are reported (i.e., > 500 days or < -500 days).

In addition, we test the improvement of the lag measurements by using subsamples of the 6-year light curves, finding that cross-correlation results are more reliable with higher cross-correlation coefficients, because of the densely distributed observations in particular seasons. Note that the total 6-year light curve is composed of six seasons separated by seasonal gaps. Specifically, we find an improvement relative to the total light curves when we use only 2018 observations for J0939+375, 2020-2021 observations for J1203+455, 2016-2017 observations for PG 1545+210, and 2019-2021 observations for PG 1427+480, presumably owing to the much higher quality light curves during these specific seasons. Under such circumstances, we adopt the measurements based on the light curves of these specific seasons.

Both the posterior distributions of ICCF and JAVELIN can show multiple peaks as a feature of sparsely sampled multiple-year data with seasonal gaps (e.g., Grier et al. 2019; Homayouni et al. 2020; Yu et al. 2022), which is likely to be caused by quasi-periodic variations, mismatch of weakly variable features (Homayouni et al. 2020), and seasonal gaps. Following Grier et al. (2019), we employ an alias identification procedure to remove these aliases and identify the primary peak for measuring lags. We apply a weight function to the posterior distribution of ICCF and JAVELIN, which is a convolution of the following two components. The first component is a probability function based on the overlapped fraction defined as:

$$P(\tau) = [N(\tau)/N(0)]^2, \quad (6)$$

where $N(\tau)$ and $N(0)$ is the number of overlapped points between continuum and emission-line light curves with or without shifting one light curve by τ , respectively. This component helps to reduce the weight of the lag values that are similar to seasonal gaps because no real data are overlapped between the light curves of the continuum and $H\beta$ if one light curve is shifted by these values. The second component is the auto-correlation function (ACF), which represents how fast the contin-

uum variability is. If the continuum light curve varies slowly, then the distribution of ACF is wide, indicating that the seasonal gaps are less likely to affect the lag measurement. On the other hand, fast continuum variability leads to a narrow ACF distribution, and in this case, the important features of the variability pattern are more likely blocked by the seasonal gaps (Homayouni et al. 2020). Thus, we combine the overlap probability function (i.e., Eq. 6) and the ACF to generate a weight function, which then is multiplied by the lag posterior distribution of ICCF and JAVELIN.

To identify the primary peaks in the weighted posterior distribution, we first smooth the distribution by a Gaussian kernel with a width of 12 days, which was determined based on experiments and visual inspection as similarly adopted by previous studies (e.g., Grier et al. 2019; Homayouni et al. 2020; Yu et al. 2022). By identifying the highest peak as the primary peak in the smoothed distribution, we define its range between the two adjacent local minimums. Then, we remove the posteriors outside this range and measure the lag from the truncated distribution. Note that we use the weighted posterior distribution for defining the range of truncation. Finally, we determine the lag and its uncertainty by measuring the median and 16-to-84th quadrature of the truncated *unweighted* posterior distribution.

Based on the aforementioned analysis, we measure the $H\beta$ lag of the sample (see Table 5). As a consistency check, we compare the new measurements with the measurements presented in Paper II, which reported the initial $H\beta$ lag measurements of two AGNs, J0801+512 (2MASS J10261389+5237510) and J1619+501 based on the first-three-year data. The lags measured in Paper II are $41.8^{+4.9}_{-6.0}$ days and $60.1^{+33.1}_{-19.0}$ days in the observed frame for J0801+512 and J1619+501, respectively. Our new lag measurement of J0801+512 ($43.2^{+4.7}_{-4.8}$ days) is consistent with the measurement reported in Paper II within 1σ uncertainty, while for J1619+501 our new measurement ($39.3^{+8.6}_{-8.7}$ days) is much smaller but consistent with Paper II considering the large uncertainty of the initial measurement.

4.2. Effect of detrending

A long-term trend in the line light curves can bias the cross-correlation result because the long-timescale (low frequency) trend can overwhelm the relatively shorter intrinsic pattern due to the lag (e.g., Welsh 1999; Denney et al. 2010; Zhang et al. 2019). In such cases, detrending of the light curves may improve the lag analysis.

We examine the effect of long-term trends by detrending the continuum and/or $H\beta$ light curves using a first-order polynomial, which is usually enough to remove the

various linear trends between the continuum and emission line light curves. Higher order polynomials are more dangerous to use since they are suspected to introduce artificial signals in the light curves and largely reduce the cross-correlation strength at the same time (Peterson et al. 1995). We find that only for two objects, PG 1100+772 and PG 1202+281, r_{\max} is significantly improved after detrending. Thus, we decide to use the results based on detrending for the two objects. For completeness, we present the lag analysis for these two objects without detrending in Appendix A.

Based on the optical and radio variability of a radio-loud AGN, 3C 273, Li et al. (2020) suggested that the underlying physics of the detrending process is to correct for the contamination of jet emission in the optical continuum light curves since jet emission has no corresponding effect on the emission-line light curves. We note that PG 1100+772 is a radio-loud AGN with a radio loudness $R = f_{5\text{GHz}}/f_{2500} \sim 400$, suggesting that PG 1100+772 can be treated as an analogy of 3C 273 (Zhang et al. 2019). However, it is difficult to disentangle the jet contribution from the observed continuum light curves for this target due to the lack of radio monitoring data during our reverberation campaign. It is possible that radio-loud AGNs may introduce scatter in the size-luminosity relation if this scenario is correct. A larger sample of radio-loud AGNs is required in the RM studies to verify this scenario.

4.3. Lag reliability

In this section, we investigate the reliability of the lag measurements from the cross-correlation analysis. The two main criteria of lag reliability are the goodness of the cross-correlation between the continuum and emission line light curves, and the constraints against artificial signatures in the light curves, i.e., aliases. In general, the lag measurements are more reliable if the input light curves have a higher cadence, more regular sampling, longer time baseline, and stronger non-quasi-periodic variability patterns. However, well-defined quantitative criteria are yet to be available while a few new attempts have been reported in the literature.

One of the criteria of reliability is the maximum cross-correlation coefficient r_{\max} , which is the maximum value in the ICCF, representing the strength of the correlation between two light curves. Previous studies often used a threshold of $r_{\max} > 0.6$ or 0.5 , to adopt reliable lag measurements (e.g. Grier et al. 2017; U et al. 2022). However, r_{\max} alone is not sufficient to determine the lag reliability. For instance, r_{\max} would be relatively high even though the light curves have very few data points but show strong linear variation, or even if the variability

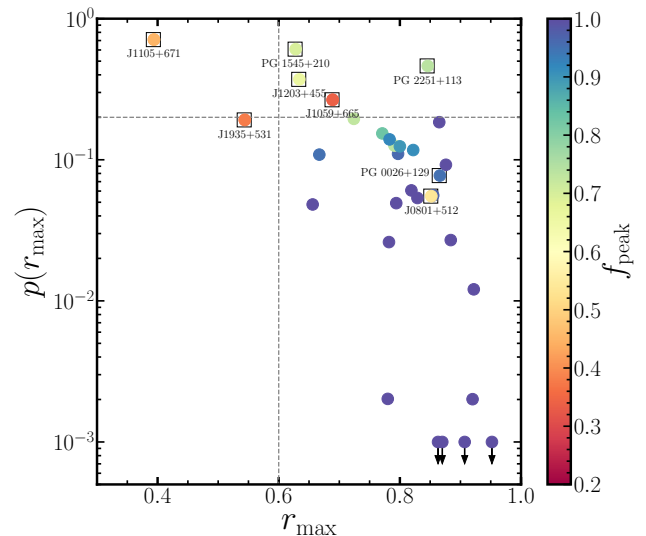


Figure 15. Assessment of the lag reliability using the three criteria, i.e., the maximum cross-correlation coefficient (r_{\max}), the probability that uncorrelated light curves would produce a cross-correlation coefficient of at least r_{\max} ($p(r_{\max})$), and the fraction of the primary peak in the posterior distribution (f_{peak}). The best lags are defined with $r_{\max} \geq 0.6$ (vertical dashed line), $p(r_{\max}) < 0.2$ (horizontal dashed line), and $f_{\text{peak}} > 0.6$. Two objects show $r_{\max} < 0.6$. There are four objects with $r_{\max} \geq 0.6$, that do not satisfy $p(r_{\max}) < 0.2$, and there is one object with $r_{\max} \geq 0.6$ and $p(r_{\max}) < 0.2$, but with $f_{\text{peak}} \leq 0.6$.

amplitude is small compared to the flux uncertainties, but some features in the light curves are well matched. In these cases, the measured lag can be biased or reflect the randomly uncorrelated light curves. Not to mention that flux uncertainties are not taken into account in the r_{\max} calculation.

Recently, a new method PyI²CCF⁹ has been proposed to assess the lag reliability (Guo & Barth 2021; U et al. 2022, Guo et al., in prep), using a null-hypothesis to evaluate the probability that the observed cross-correlation can be equally obtained by two uncorrelated red-noise light curves. This idea originates from X-ray reverberation studies and has been used to assess the correlation of multi-wavelength variability of AGNs (Uttley et al. 2003; Arévalo et al. 2008; Chatterjee et al. 2008). Using the publicly available PyI²CCF, we investigate the reliability of our lag measurements. We generate 10^3 realizations of a pair of mock light curves for each object by keeping the same cadence and sampling as the observed light curves using DRW models. Then, by counting the number of positive lags ($\tau > 0$) with the r_{\max} value higher than the observed r_{\max} among all

⁹ <https://github.com/legolason/PyI2CCF>

simulations, we determine the probability $p(r_{\max})_{\tau>0}$ as a lag significant indicator. In this process, we keep the aforementioned searching window as defined in §4.1.

We further examine the fraction of the primary peak (f_{peak}) in the posterior distribution that describes how much of the posteriors are within the range of the primary peak. For example, f_{peak} less than 0.6 is often considered as that there are possible significant solutions other than the identified primary peak (Grier et al. 2019; Homayouni et al. 2020; Yu et al. 2022; Malik et al. 2022). We listed f_{peak} of τ_{cent} of all targets in Table 5.

We present the three criteria of the lag reliability: r_{\max} based on the observed light curves, $p(r_{\max})$ based on simulations, and f_{peak} calculated from the posterior distribution, for individual AGNs in Table 5. Note that for the majority of our targets, the measured lag is reliable based on these three assessments. In Figure 15 we directly compare the two indicators, i.e., r_{\max} and $p(r_{\max})$ along with the color-coded (f_{peak}). We quantitatively define the best lag measurements, by requiring $r_{\max} \geq 0.6$, $p(r_{\max}) \leq 0.2$, and $f_{\text{peak}} \geq 0.6$. Note that there is no strict cutoff of $p(r_{\max})$ between best and less-reliable lag measurements. We adopt $p(r_{\max})_{\tau>0} \leq 0.2$ following the previous study by U et al. (2022). In these assessments, we find that the measured lag of seven targets, namely, J0801+512, J1059+665, J1105+671, J1203+455, PG 1545+210, J1935+531, and PG 2251+113, do not satisfy the lag reliability criteria. By excluding these seven targets, we obtain the best H β lag measurements for 25 AGNs. In the case of PG 0026+129, the obtained lag is consistent with zero within 1σ uncertainty, suggesting that the lag is not resolved.

Finally, we perform a visual inspection of all light curves to check how well the continuum light curve matches the emission-line light curve after shifting the continuum light curve by the measured lag. This method is qualitative, providing an additional check on the reliability of the measured lag. We present the two light curves, after shifting by the lag and scaling with the median and standard deviation of the fluxes, in the lower panel of each target in Figure 4. Overall, we find a good match between the shifted continuum and the H β light curves of the majority of targets in the sample, confirming the reliability of the lag measurements.

As a consistency check, we compare the ICCF and JAVELIN measurements in Figure 16, finding that they are generally consistent. However, six objects, namely, Mrk 1501, J1026+523, J1059+665, J1105+671, PG 1322+659, and PG 2251+113, show a large discrepancy with JAVELIN lag larger than ICCF lag by 150 days or smaller than by -150 days while ICCF lags

are within $[0, 100]$ days. Three of them are already identified as less-reliable, for the other three AGNs the JAVELIN lag seems overestimated or underestimated because of the combined effect of seasonal gaps and quasi-periodic variability based on visual inspection of their light curves. This result suggests that although the typical error of JAVELIN lag is indeed smaller than ICCF, JAVELIN measurements are sometimes easier to be affected by seasonal gaps than ICCF and generate spurious measurements, particularly for sparsely sampled light curves. Thus, we decided not to disqualify these ICCF lags as unreliable, albeit with the discrepancy with the JAVELIN results.

A simple statistical approach to quantify the lag reliability of a given sample is to examine the sample's false positive rate, i.e., what fraction of the lag measurements is false detection caused by inopportune features, seasonal gaps as well as inappropriately identified primary peaks and alias identification. The incidence of negative lags over the entire sample can be an indicator of the false positive rate (e.g., Shen et al. 2016; Grier et al. 2017, 2019). In our SAMP sample, there is one object with a negative τ_{cent} and one object with a negative τ_{JAV} . If we conservatively count these two measurements, the false positive rate is $\sim 6\%$ of the SAMP sample, indicating the high quality of our lag measurements.

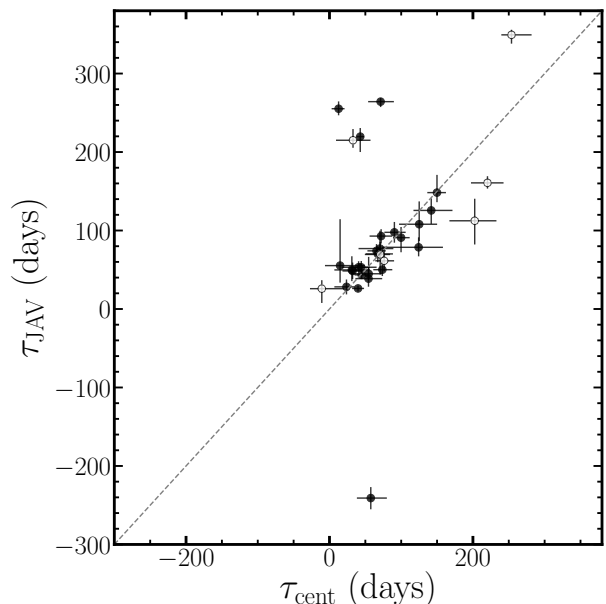


Figure 16. Comparison of the lag measurements in the observed-frame between τ_{cent} (ICCF) and τ_{JAV} (JAVELIN). Best and less-reliable lag measurements are denoted with filled and open circles, respectively, using the threshold of $r_{\max} = 0.6$, $p(r_{\max}) = 0.2$ and $f_{\text{peak}} = 0.6$.

Table 5. Observed-frame lags and lag reliability parameters

Name	τ_{cent} (days)	τ_{peak} (days)	τ_{JAV} (days)	r_{max}	$p(r_{\text{max}})$	f_{peak}
(1)	(2)	(3)	(4)	(5)	(6)	(7)
1 Mrk 1501	12.7 ^{+8.3} _{-9.7}	24.0 ^{+4.0} _{-9.0}	255.2 ^{+9.3} _{-8.4}	0.85	0.056	0.97
2 PG 0026+129	14.8 ^{+34.5} _{-21.1}	25.0 ^{+19.0} _{-18.0}	55.3 ^{+59.1} _{-21.7}	0.87	0.077	0.95
3 PG 0052+251	73.7 ^{+13.9} _{-12.6}	59.0 ^{+16.0} _{-14.0}	50.1 ^{+11.4} _{-8.1}	0.95	< 0.001	1.00
4 J0101+422	90.5 ^{+15.7} _{-14.0}	91.0 ^{+30.0} _{-40.0}	97.7 ^{+13.2} _{-13.2}	0.80	0.110	0.96
5 J0140+234	149.9 ^{+12.5} _{-13.5}	148.0 ^{+34.0} _{-22.0}	148.3 ^{+22.6} _{-12.2}	0.92	0.002	1.00
6 Mrk 1014	125.1 ^{+25.0} _{-28.1}	145.0 ^{+22.0} _{-22.7}	108.0 ^{+29.1} _{-21.4}	0.92	0.012	1.00
8 J0939+375*	23.7 ^{+11.2} _{-16.9}	26.0 ^{+9.0} _{-23.0}	28.2 ^{+9.6} _{-9.4}	0.86	0.185	1.00
9 PG 0947+396	44.3 ^{+11.5} _{-13.3}	41.0 ^{+17.0} _{-16.0}	53.1 ^{+8.1} _{-7.1}	0.78	0.026	1.00
10 J1026+523	42.9 ^{+5.3} _{-5.0}	34.0 ^{+9.0} _{-7.0}	219.6 ^{+11.0} _{-19.6}	0.86	< 0.001	1.00
12 PG 1100+772	70.4 ^{+18.7} _{-29.9}	79.0 ^{+16.7} _{-25.2}	77.0 ^{+22.7} _{-12.8}	0.67	0.109	0.95
14 J1120+423	54.4 ^{+19.1} _{-18.3}	35.0 ^{+17.0} _{-12.0}	38.7 ^{+14.9} _{-10.3}	0.91	< 0.001	1.00
15 PG 1121+422	141.9 ^{+29.6} _{-24.8}	151.0 ^{+29.0} _{-29.0}	125.6 ^{+15.4} _{-17.2}	0.82	0.061	1.00
17 PG 1202+281	44.9 ^{+10.6} _{-9.9}	40.0 ^{+7.0} _{-9.0}	43.5 ^{+5.5} _{-5.0}	0.66	0.048	1.00
18 J1217+333	31.2 ^{+25.0} _{-24.4}	38.0 ^{+33.0} _{-27.5}	49.8 ^{+17.4} _{-14.3}	0.79	0.126	0.74
19 VIII Zw 218	71.3 ^{+18.5} _{-17.4}	69.0 ^{+16.0} _{-30.0}	264.2 ^{+4.6} _{-6.9}	0.72	0.195	0.73
20 PG 1322+659	57.6 ^{+22.4} _{-19.4}	52.0 ^{+15.0} _{-29.0}	-240.9 ^{+14.0} _{-14.3}	0.78	0.139	0.92
21 J1415+483	32.2 ^{+15.0} _{-14.1}	36.0 ^{+14.0} _{-14.0}	48.5 ^{+10.7} _{-10.3}	0.80	0.124	0.90
22 PG 1427+480*	40.6 ^{+25.1} _{-23.7}	50.0 ^{+28.0} _{-36.0}	53.2 ^{+7.7} _{-6.3}	0.88	0.092	1.00
23 PG 1440+356	54.6 ^{+18.2} _{-22.6}	44.0 ^{+6.0} _{-20.9}	44.9 ^{+21.5} _{-7.4}	0.87	< 0.001	1.00
24 J1456+380	99.8 ^{+12.0} _{-11.2}	58.0 ^{+9.0} _{-16.5}	90.9 ^{+13.6} _{-18.6}	0.83	0.054	1.00
25 J1526+275	124.3 ^{+33.9} _{-51.4}	80.0 ^{+11.0} _{-22.0}	78.6 ^{+12.7} _{-11.5}	0.77	0.154	0.83
26 J1540+355	67.4 ^{+21.1} _{-17.0}	50.0 ^{+15.0} _{-12.6}	70.2 ^{+9.4} _{-10.6}	0.79	0.049	1.00
28 PG 1612+261	72.0 ^{+15.4} _{-16.1}	76.0 ^{+16.0} _{-19.0}	92.9 ^{+8.8} _{-9.5}	0.82	0.117	0.91
29 J1619+501	39.8 ^{+8.4} _{-8.3}	30.0 ^{+20.0} _{-6.0}	26.2 ^{+3.3} _{-3.7}	0.78	0.002	1.00
32 PG 2349-014	65.6 ^{+12.9} _{-12.7}	66.0 ^{+12.0} _{-10.0}	74.1 ^{+8.6} _{-5.1}	0.88	0.027	1.00
7 J0801+512	220.3 ^{+22.4} _{-23.0}	165.0 ^{+10.0} _{-12.0}	160.7 ^{+8.5} _{-7.3}	0.85	0.055	0.54
11 J1059+665	253.8 ^{+28.0} _{-14.2}	259.5 ^{+21.9} _{-8.5}	349.3 ^{+6.5} _{-11.2}	0.69	0.266	0.34
13 J1105+671	32.8 ^{+24.4} _{-23.7}	25.0 ^{+27.2} _{-17.2}	215.0 ^{+14.3} _{-9.6}	0.39	0.711	0.45
16 J1203+455*	70.7 ^{+13.8} _{-21.4}	68.0 ^{+18.0} _{-20.0}	69.5 ^{+15.9} _{-25.5}	0.63	0.372	0.66
27 PG 1545+210*	76.2 ^{+13.9} _{-12.4}	74.0 ^{+20.0} _{-13.0}	61.4 ^{+17.8} _{-13.3}	0.63	0.608	0.70
30 J1935+531	-10.7 ^{+31.3} _{-16.5}	-19.0 ^{+16.0} _{-8.4}	25.9 ^{+10.8} _{-18.2}	0.54	0.192	0.38
31 PG 2251+113	202.5 ^{+30.3} _{-35.3}	268.0 ^{+6.6} _{-12.0}	112.4 ^{+28.1} _{-30.2}	0.85	0.463	0.74

Notes. Notes. Column (1): object names; Column (2)–(4): the observed-frame lags of ICCF centroid (τ_{cent}), peak (τ_{peak}), and JAVELIN, respectively, through weighting and alias removal procedure. The lags and their two uncertainties are determined from the median, and 16th-50th/84-50th percentile interval from the unweighted lag posterior distribution covered by the primary peak. For targets with * sign, lags are calculated based on the part of the light curves; Column (5)–(8): lag reliability parameters: r_{max} represents the maximum correlation coefficient; $p(r_{\text{max}})$ is derived from PyI²CCF simulation which indicates how large the chance is to obtain the observed r_{max} from random light curves; f_{peak} is the fraction of the posterior distribution within the selected primary peak. Seven objects with less reliable lag measurements indicated by $r_{\text{max}} \leq 0.6$, $p(r_{\text{max}}) \geq 0.2$, or $f_{\text{peak}} \leq 0.6$ are listed in the bottom.

4.4. BH mass and Eddington ratio

In this section, we present the M_{BH} determination of the sample, by measuring the width of the $\text{H}\beta$ emission line. We also determine Eddington ratio of individual AGNs using continuum luminosity. We compare the distribution of M_{BH} , luminosity, and Eddington ratio of the SAMP AGNs with that of the previous reverberation-mapped AGNs.

4.4.1. $\text{H}\beta$ line width measurements

We measure the $\text{H}\beta$ line width from the decomposed broad $\text{H}\beta$ emission line profile using the mean spectra as well as the broad-line-only rms spectra. As a velocity measure, we adopt the full-width-at-half-maximum (FWHM) and the line dispersion σ_{line} (the 2nd moment of the line profile), following the definition by Peterson et al. (2004). Note that we conservatively define two windows to represent the local continuum in the rms spectra for line width measurements as shown in Figure 2. Using the measured instrumental resolution of 481 km s^{-1} from skylines, we correct for the instrumental broadening by subtracting the instrumental resolution from the measured widths in quadrature. Since the spectral resolution is measured from skylines, which uniformly fill the $4''$ slit, the actual resolution for a point source is likely to be smaller. However, this effect is insignificant because $\text{H}\beta$ lines are intrinsically very broad. Since the change of the instrumental broadening during our observations is relatively small compared to the broad line width, we adopt a single representative spectral resolution, 481 km s^{-1} .

4.4.2. M_{BH} measurements

We determine the M_{BH} based on Eq. 1, using the τ_{cent} from the ICCF analysis as the lag and the line dispersion of $\text{H}\beta$ measured from the rms spectra (σ_{rms}) as the velocity along with the average $f = 4.47 \pm 0.43$ (Woo et al. 2015). Note that while we adopt a single f value in this work, we will present the velocity-resolved lag measurements and dynamical modeling to derive the f factor for each AGN in the future.

For determining M_{BH} , the line dispersion (σ_{rms}) is commonly used in RM studies because it best recovers the virial relation (Peterson et al. 2004; Park et al. 2012b). It is also suggested that the line dispersion is less sensitive to other factors, e.g., orientation, compared to the FWHM (Collin et al. 2006; Wang et al. 2019). On the other hand, the FWHM is frequently used in single-epoch M_{BH} estimation as it is easier to measure than the line dispersion based on low S/N spectra. We provide the M_{BH} of the sample based on the line dispersion in Table 6, but the M_{BH} with FWHM can be easily derived using Table 6.

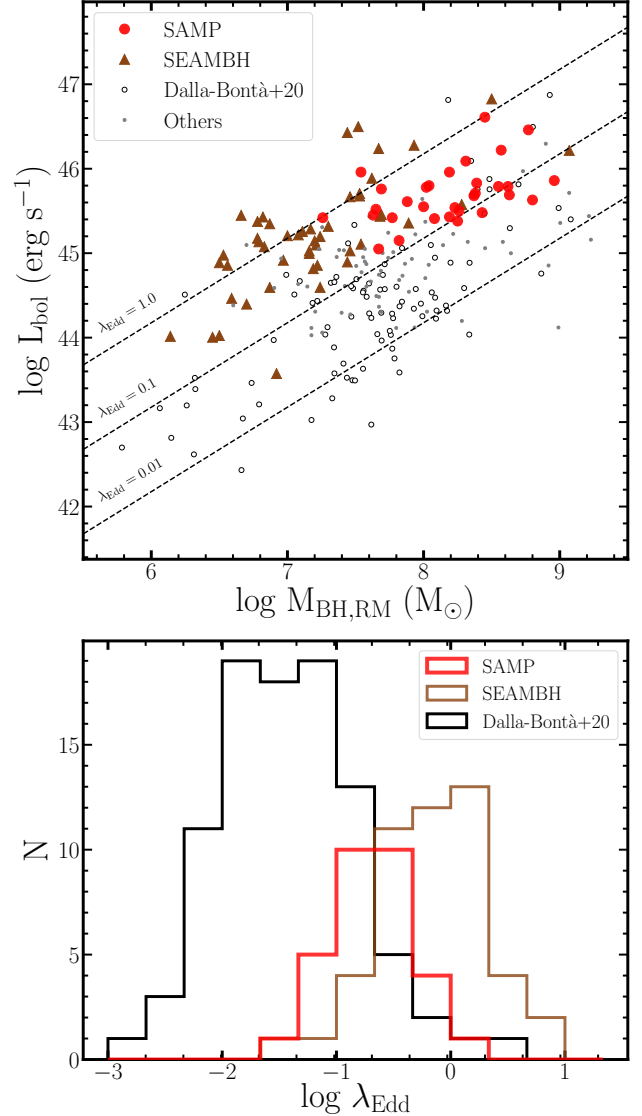


Figure 17. Upper: The distribution of SAMP final sample (red circle) on the BH mass–bolometric luminosity plane, overplotted with Dalla Bontà et al. (2020) collections (black dots) and SEAMBHs (Du & Wang 2019; Hu et al. 2021; Li et al. 2021, brown triangles). Three dashed lines indicate the Eddington ratios from 0.01, 0.1, to 1.0 as labeled in the left end above the line. Our SAMP final sample has moderately high Eddington ratios. Lower: The distribution of Eddington ratios for SAMP, and other samples.

We also estimate the bolometric luminosity using the monochromatic luminosity L_{5100} along with a constant bolometric correction factor $\kappa = 9.26$ (e.g., Richards et al. 2006; Shen et al. 2011). For calculating the Eddington luminosity L_{Edd} , we assume $L_{\text{Edd}} = 1.3 \times 10^{38} M_{\text{BH}}/M_{\odot}$.

In Figure 17 we present M_{BH} and bolometric luminosity of the sample, in comparison with those of the pre-

Table 6. Final Rest-Frame Lags, AGN luminosities, Line Widths, Virial Products, and Black Masses

Name	τ_{final} (days)	$L_{5100, \text{AGN}}$ ($10^{44} \text{ erg s}^{-1}$)	$\text{FWHM}_{\text{mean}}$ (km s^{-1})	σ_{mean} (km s^{-1})	FWHM_{rms} (km s^{-1})	σ_{rms} (km s^{-1})	$\text{VP}_{\sigma_{\text{rms}}}$ ($\times 10^7 M_{\odot}$)	M_{BH} ($\times 10^8 M_{\odot}$)	
(1)	(2)	(3)	(4)	(5)	(6)	(7)	(8)	(9)	
1	Mrk 1501	$11.7^{+7.6}_{-8.9}$	1.22 ± 0.06	4662 ± 93	1935 ± 30	4290 ± 375	2154 ± 64	$1.1^{+0.7}_{-0.8}$	$0.5^{+0.3}_{-0.4}$
2	PG 0026+129	$13.0^{+30.2}_{-18.5}$	9.81 ± 0.24	2608 ± 62	2471 ± 42	1334 ± 216	1756 ± 212	$0.8^{+1.8}_{-1.1}$	$0.3^{+0.8}_{-0.5}$
3	PG 0052+251	$63.9^{+12.0}_{-10.9}$	5.58 ± 0.16	4724 ± 62	2196 ± 19	4104 ± 622	2068 ± 267	$5.3^{+1.0}_{-0.9}$	$2.4^{+0.5}_{-0.5}$
4	J0101+422	$76.1^{+13.2}_{-11.8}$	6.67 ± 0.12	6171 ± 31	2514 ± 62	5406 ± 278	2300 ± 143	$7.8^{+1.4}_{-1.2}$	$3.5^{+0.7}_{-0.7}$
5	J0140+234	$113.6^{+9.5}_{-10.2}$	13.35 ± 0.14	2896 ± 62	1601 ± 12	2230 ± 97	1438 ± 138	$4.6^{+0.4}_{-0.4}$	$2.0^{+0.3}_{-0.3}$
6	Mrk 1014	$107.6^{+21.5}_{-24.2}$	7.37 ± 0.33	2890 ± 97	1730 ± 153	1786 ± 67	1618 ± 110	$5.5^{+1.1}_{-1.2}$	$2.5^{+0.6}_{-0.6}$
8	J0939+375	$19.3^{+9.1}_{-13.7}$	2.85 ± 0.07	2921 ± 154	1561 ± 39	1400 ± 67	1038 ± 113	$0.4^{+0.2}_{-0.3}$	$0.2^{+0.1}_{-0.1}$
9	PG 0947+396	$36.7^{+9.5}_{-11.0}$	3.78 ± 0.10	5258 ± 36	2396 ± 16	4910 ± 648	2294 ± 192	$3.8^{+1.0}_{-1.1}$	$1.7^{+0.5}_{-0.6}$
10	J1026+523	$34.1^{+4.2}_{-4.0}$	3.04 ± 0.07	3822 ± 31	1938 ± 7	2608 ± 154	1198 ± 66	$0.9^{+0.1}_{-0.1}$	$0.4^{+0.1}_{-0.1}$
12	PG 1100+772	$53.7^{+14.3}_{-22.8}$	44.05 ± 1.24	5993 ± 62	2465 ± 166	5591 ± 154	2445 ± 56	$6.3^{+1.7}_{-2.7}$	$2.8^{+0.8}_{-1.2}$
14	J1120+423	$44.4^{+15.6}_{-14.9}$	3.38 ± 0.10	6211 ± 31	2466 ± 11	5158 ± 278	2180 ± 45	$4.1^{+1.4}_{-1.4}$	$1.8^{+0.7}_{-0.7}$
15	PG 1121+422	$115.8^{+24.2}_{-20.2}$	6.86 ± 0.10	2613 ± 31	1627 ± 10	2230 ± 62	1037 ± 70	$2.4^{+0.5}_{-0.4}$	$1.1^{+0.3}_{-0.2}$
17	PG 1202+281	$38.5^{+9.1}_{-8.5}$	2.75 ± 0.05	5545 ± 62	2503 ± 25	3855 ± 411	1893 ± 111	$2.7^{+0.6}_{-0.6}$	$1.2^{+0.3}_{-0.3}$
18	J1217+333	$26.5^{+21.2}_{-20.7}$	1.53 ± 0.08	4476 ± 31	1971 ± 18	3233 ± 154	1691 ± 54	$1.5^{+1.2}_{-1.2}$	$0.7^{+0.5}_{-0.5}$
19	VIII Zw 218	$63.3^{+16.4}_{-15.4}$	2.90 ± 0.05	5371 ± 62	2523 ± 21	3980 ± 185	1679 ± 113	$3.5^{+0.9}_{-0.8}$	$1.6^{+0.4}_{-0.4}$
20	PG 1322+659	$49.3^{+19.2}_{-16.6}$	6.48 ± 0.14	3004 ± 31	1583 ± 12	2104 ± 97	1560 ± 45	$2.3^{+0.9}_{-0.8}$	$1.1^{+0.4}_{-0.4}$
21	J1415+483	$25.3^{+11.8}_{-11.1}$	4.41 ± 0.11	3654 ± 62	1742 ± 16	4166 ± 1172	1847 ± 343	$1.7^{+0.8}_{-0.7}$	$0.8^{+0.4}_{-0.3}$
22	PG 1427+480	$33.3^{+20.6}_{-19.4}$	6.26 ± 0.12	2721 ± 97	1582 ± 38	1786 ± 93	1292 ± 155	$1.1^{+0.7}_{-0.6}$	$0.5^{+0.3}_{-0.3}$
23	PG 1440+356	$50.6^{+16.9}_{-20.9}$	3.61 ± 0.05	2545 ± 62	1263 ± 15	2167 ± 97	1003 ± 113	$1.0^{+0.3}_{-0.4}$	$0.4^{+0.2}_{-0.2}$
24	J1456+380	$77.8^{+9.4}_{-8.7}$	5.32 ± 0.11	7972 ± 154	3002 ± 72	5901 ± 776	2504 ± 167	$9.5^{+1.1}_{-1.1}$	$4.3^{+0.7}_{-0.7}$
25	J1526+275	$63.9^{+10.3}_{-9.3}$	6.61 ± 0.10	4538 ± 31	1970 ± 12	4476 ± 216	2173 ± 101	$9.3^{+2.5}_{-3.9}$	$4.2^{+1.2}_{-1.8}$
26	J1540+355	$57.9^{+18.1}_{-14.6}$	2.83 ± 0.06	2383 ± 62	1493 ± 14	2041 ± 93	1077 ± 79	$1.3^{+0.4}_{-0.3}$	$0.6^{+0.2}_{-0.2}$
28	PG 1612+261	$63.7^{+13.6}_{-14.2}$	5.12 ± 0.21	3165 ± 93	1887 ± 48	1977 ± 195	2054 ± 265	$5.2^{+1.1}_{-1.2}$	$2.3^{+0.6}_{-0.6}$
29	J1619+501	$32.3^{+6.8}_{-6.7}$	2.62 ± 0.04	5391 ± 62	2388 ± 17	6519 ± 437	2511 ± 367	$4.0^{+0.8}_{-0.8}$	$1.8^{+0.4}_{-0.4}$
32	PG 2349-014	$55.9^{+11.0}_{-10.8}$	4.58 ± 0.16	6924 ± 123	3841 ± 87	6890 ± 555	3595 ± 197	$14.1^{+2.8}_{-2.7}$	$6.3^{+1.4}_{-1.4}$
7	J0801+512	$166.8^{+17.0}_{-17.4}$	3.24 ± 0.08	2274 ± 62	1469 ± 23	1400 ± 221	1359 ± 157	$6.0^{+0.6}_{-0.6}$	$2.7^{+0.4}_{-0.4}$
11	J1059+665	$189.4^{+20.9}_{-10.6}$	7.86 ± 0.17	4457 ± 62	2210 ± 25	5034 ± 1120	2343 ± 150	$20.3^{+2.2}_{-1.1}$	$9.1^{+1.5}_{-1.2}$
13	J1105+671	$24.8^{+18.5}_{-18.0}$	3.83 ± 0.08	4724 ± 62	2192 ± 37	3793 ± 807	2145 ± 298	$2.2^{+1.7}_{-1.6}$	$1.0^{+0.8}_{-0.7}$
16	J1203+455	$52.6^{+10.3}_{-15.9}$	9.79 ± 0.17	5653 ± 93	2854 ± 42	4290 ± 308	1840 ± 154	$3.5^{+0.7}_{-1.1}$	$1.6^{+0.4}_{-0.5}$
27	PG 1545+210	$60.3^{+11.0}_{-9.8}$	17.95 ± 0.27	6557 ± 93	2932 ± 24	5282 ± 1955	2655 ± 193	$8.3^{+1.5}_{-1.4}$	$3.7^{+0.8}_{-0.8}$
30	J1935+531	...	13.77 ± 0.20	5284 ± 159	2705 ± 45	2921 ± 349	2361 ± 157
31	PG 2251+113	$152.7^{+22.9}_{-26.6}$	30.91 ± 0.43	4811 ± 31	2752 ± 18	5034 ± 252	2103 ± 92	$13.2^{+2.0}_{-2.3}$	$5.9^{+1.1}_{-1.2}$

Notes. Column (1): object names; Column (2): the final rest-frame lags. We adopt the ICCF τ_{cent} for all objects except J1526+275 for which we prefer τ_{JAV} as the final lag measurement (see §4.3). Six unreliable measurements are listed at the bottom with one object showing negative lags not displayed. Column (3): extinction corrected and host contamination removed (if any) AGN luminosities in the unit of $10^{44} \text{ erg s}^{-1}$; Column (4)-(5): FWHM and σ_{line} measured from mean spectrum; Column (6)-(7): FWHM and σ_{line} measured from rms spectrum; Column (8): virial products calculated using the final lags in Column (2) and the rms spectrum σ_{line} in Column (7); Column (8): final BH masses calculated by multiplying the virial products in Column (7) with the virial factor $f = 4.47$ (Woo et al. 2015).

viously reverberation-mapped AGNs by combining the collection of Dalla Bontà et al. (2020) and the AGNs from the SEAMBHs (Du & Wang 2019; Hu et al. 2021; Li et al. 2021). The M_{BH} of the SAMP AGNs range from 10^7 to $10^9 M_{\odot}$ and the Eddington ratio covers from 0.05 to 1.82 with a median of 0.17, which is higher than that of the sample of Dalla Bontà et al. (2020) but lower than the AGN in SEAMBHs.

5. DISCUSSION

5.1. $H\beta$ BLR size-luminosity relation

As the number of $H\beta$ lag measurements increased over the last decade, it has been demonstrated that the $H\beta$ size–luminosity relation has a considerably larger scatter and a shallower slope than previously accepted, indicating a more complex nature of the relation (e.g., Du et al. 2016; Grier et al. 2017; Du et al. 2018a; Du & Wang 2019; Martínez-Aldama et al. 2019; Hu et al. 2021; Li et al. 2021). In particular, it is claimed that super-Eddington AGNs tend to be systematically offset from the relation of lower Eddington ratio AGNs (Du et al. 2016; Li et al. 2021). In this section, we investigate the $H\beta$ BLR size-luminosity relation by combining our new measurements of high-luminosity AGNs with the previous measurements from the literature.

5.1.1. Best-fit slope and scatter

We utilize the collection by Dalla Bontà et al. (2020), who compiled a sample of AGNs with $H\beta$ lag and L_{5100} after correcting for the host galaxy contamination. As this collection does not include a large fraction of high-luminosity AGNs and AGNs without available HST images, we collect a number of AGNs from various other sources, i.e., the Super-Eddington-Accreting-Black-Holes (SEAMBHs) project (e.g., Du et al. 2016, 2018a; Hu et al. 2021; Li et al. 2021), the SDSS-RM project (Grier et al. 2017), the LAMP 2016 (U et al. 2022), and other recent studies (Li et al. 2021; Hu et al. 2021; Malik et al. 2022). The total sample consists of 242 $H\beta$ lag measurements (including multiple measurements of NGC 5548), among which 30 AGNs are based on the SAMP results. We exclude two SAMP AGNs, namely, PG 0026+129 and J1935+531, for which the obtained lag is negative or not larger than zero by 1σ uncertainty (see Table 5). Note that by adding these two AGNs, we find an insignificant change of the slope and scatter.

We perform a linear regression to derive the best-fit relation as:

$$\log[R_{\text{BLR},H\beta}/(\text{lt-day})] = K + \alpha \log[\lambda L_{5100}/(10^{44} \text{erg s}^{-1})], \quad (7)$$

where the $H\beta$ BLR size is in the unit of light days and the monochromatic luminosity λL_{5100} is expressed

in units of $10^{44} \text{erg s}^{-1}$. The α and K are the slope and intercept. To account for the asymmetric uncertainties of the lags, we performed MCMC regression fits using Python package `emcee`¹⁰, and adjusted the likelihood function so that it uses the upper error when the model value is larger than the data and uses the lower error in the opposite case. In brief, the regression minimizes the following quantity:

$$\chi^2 = \sum_{i=1}^N \frac{[y_i - (\alpha(x_i - x_0) + K)]^2}{(\alpha x)_{\text{err},i}^2 + y_{\text{err},i}^2 + \sigma_{\text{int}}^2}, \quad (8)$$

where $x_{\text{err},i}$ and $y_{\text{err},i}$ are the errors of variable x_i and y_i , respectively, x_0 is the normalization x , and the σ_{int} is the intrinsic scatter.

We obtain a best-fit slope of $0.402_{-0.022}^{+0.020}$ using the total sample of 240 AGNs with an intrinsic scatter of 0.232 dex (Figure 18 left). As we find more similarity between the SAMP and the LAMP in terms of spectroscopic observations, spectral analysis, and lag measurements, we use the combined sample of 24 best SAMP measurements (after excluding PG 0026+129 due to its unresolved lag) and 23 LAMP measurements, finding that a best-fit slope of $0.444_{-0.035}^{+0.036}$ with an intrinsic scatter of 0.177 dex (Figure 18 right and Table 7). Note that most of the SAMP objects lie below the previous relation (i.e., $\alpha = 0.533$), which was defined based on ~ 40 AGNs (~ 70 lag measurements) by Bentz et al. (2013).

It is unlikely that the deviation of the SAMP AGNs, with the observed-frame lag up to 254 days, is due to the underestimation of lags, since the SAMP results are based on the 6-year (~ 2000 days) monitoring data with a ± 600 -day lag search window. SAMP AGNs are generally luminous (i.e., $L_{5100} > 10^{44} \text{erg s}^{-1}$) and the host galaxy contamination is not significant as demonstrated by the lack of stellar absorption lines in the spectra. Based on the spectral decomposition, we measure the host fraction at 5100\AA . The average host fraction of our sample is 0.07, ranging from 0 to 0.28. Thus, the continuum luminosity is unlikely to be overestimated because of the host contribution.

Our results suggest that the slope is likely to be shallower than the popularly used 0.533 slope of Bentz et al. (2013), and that if the previous relation is utilized, single-epoch M_{BH} , particularly for high-luminosity AGNs at high- z , would be overestimated.

Note that these $H\beta$ lag measurements collected from the literature were not consistently determined since various studies adopted a number of different methods in their analysis. Thus, there could be various system-

¹⁰ <https://emcee.readthedocs.io/en/stable/>

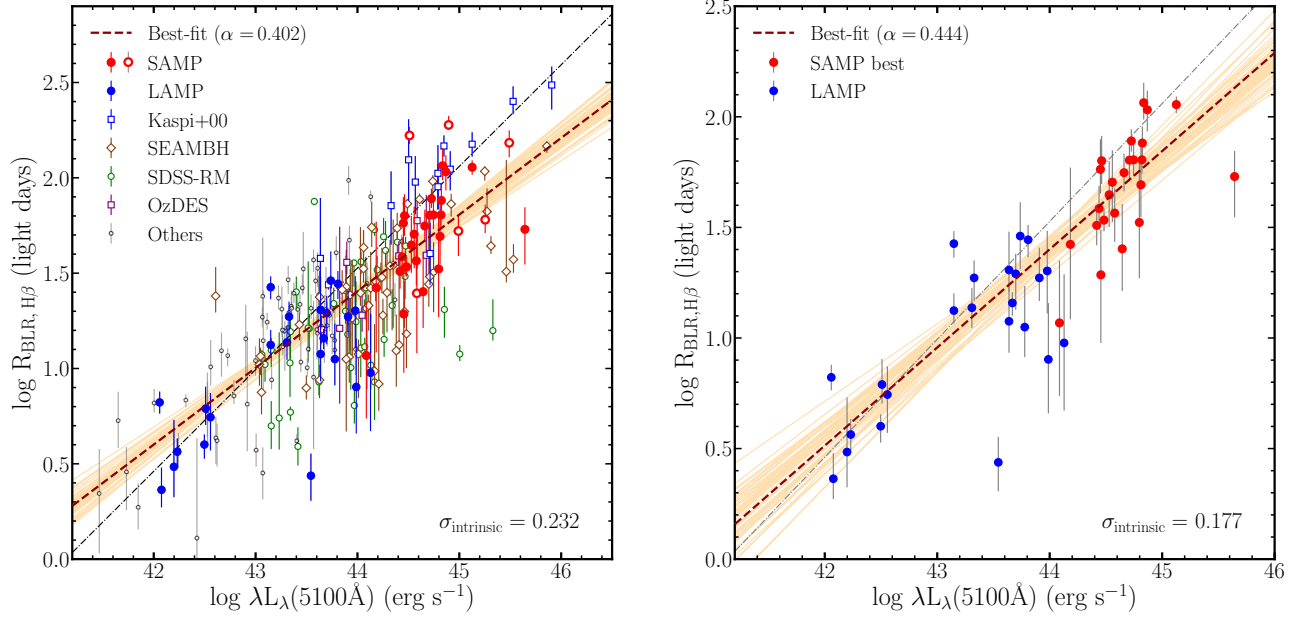


Figure 18. Left: $H\beta$ BLR size -luminosity relation of the combined sample of SAMP (red filled and open circles) and the literature measurements, including LAMP 2008, and 2016 (Bentz et al. 2009b; U et al. 2022, blue circles), 12 PG quasars from Kaspi et al. (2000) with the optical luminosity from Bentz et al. (2013) (blue open squares), SEAMBHs (Du et al. 2016, 2018a; Zhang et al. 2019; Hu et al. 2021; Li et al. 2021) (brown open square diamonds), OzDES (Malik et al. 2022) (purple open squares), SDSS-RM (Grier et al. 2017, green open circles), and others in the collection of Dalla Bontà et al. (2020) (black open circles). The brown dashed line and the light orange lines represent the best-fit relation and 50 realizations randomly drawn from the MCMC chains. As a comparison, we denote the best-fit slope of 0.533 from Bentz et al. (2013) (grey dotted-dashed line). Right: $H\beta$ BLR size -luminosity relation based on 24 best measurements from SAMP (red circles) and 23 measurements from LAMP (blue circles).

Table 7. Results of the best-fit $H\beta$ BLR size–luminosity relation

	Sample	α	K	σ
Case 1	SAMP (30) + Literature (210)	$0.402^{+0.020}_{-0.022}$	$1.405^{+0.018}_{-0.023}$	$0.232^{+0.013}_{-0.013}$
Case 2	SAMP best (24) + LAMP (23)	$0.444^{+0.036}_{-0.035}$	$1.401^{+0.034}_{-0.034}$	$0.177^{+0.028}_{-0.028}$

Note. The literature sample includes the objects from LAMP 2008 and 2016 (Bentz et al. 2009b), SEAMBH project (Du et al. 2016, 2018a; Hu et al. 2021; Li et al. 2021), SDSS-RM (Grier et al. 2017), OzDES (Malik et al. 2022), and other measurements collected by Dalla Bontà et al. (2020).

atic uncertainties in deriving the size-luminosity relation based on this heterogeneous sample. Nevertheless, we note that the best-fit relation based on the total sample is relatively tight with a rms scatter of ~ 0.3 dex and an intrinsic scatter of 0.234 dex, without requiring two different relations, respectively, for sub-Eddington and super-Eddington AGNs (c.f. Li et al. 2021). It is important to perform a consistent and uniform analysis of the cross-correlation and error measurement, in order to derive a better size-luminosity relation. We will revisit the size-luminosity relation with uniformly measured lags and investigate the systematic effect of AGN parameters on the size-luminosity relation in our next study.

5.1.2. Deviation from the size-luminosity relation

We investigate whether the deviation from the size-luminosity relation correlates with any key parameters of AGN. Using the best-fit relation obtained based on all targets (Case 1), we calculate the deviation of each target and compare with Eddington ratio in Figure 19 (right). It was previously reported that super-Eddington AGNs tend to have smaller $H\beta$ sizes for given AGN luminosity and that this deviation is stronger with higher Eddington ratios or high mass accretion rate. For example, Du et al. (2015) claimed a negative correlation between the mass accretion rate with the deviation. However, this could be naturally caused by the zone of avoidance since there is typically no type-1 AGN with

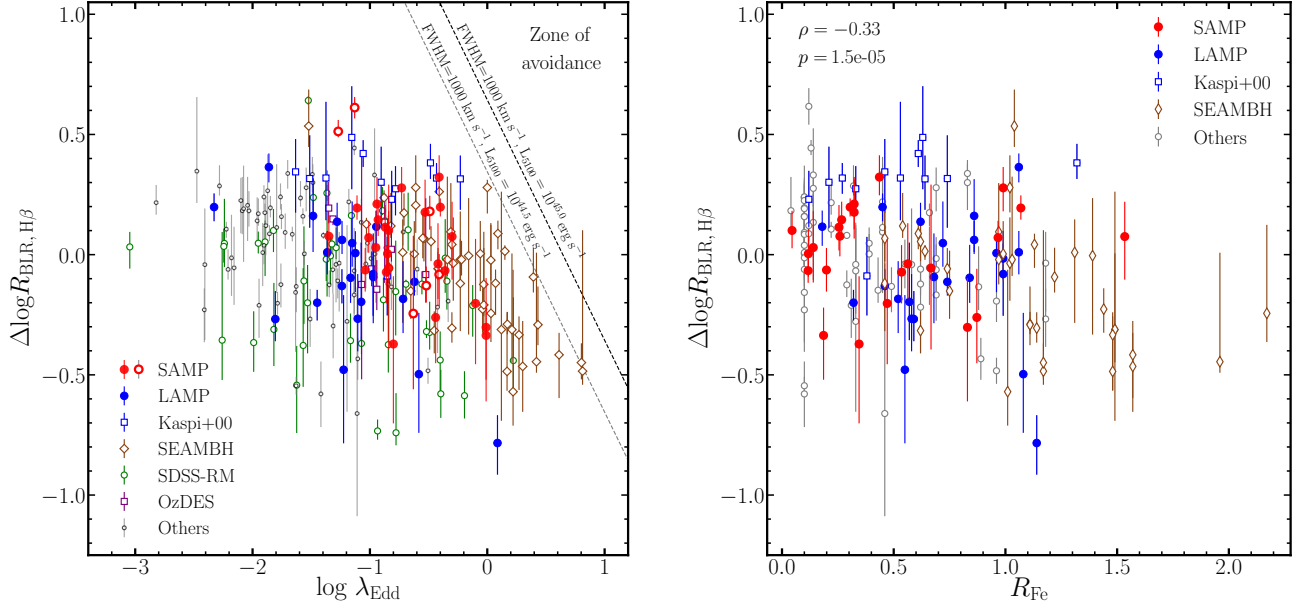


Figure 19. $H\beta$ comparison of the deviation from the size-luminosity relation with Eddington ratio (left) and strength of Fe II (right). Note that the decreasing trend with the Eddington ratio is partly due to the zone of avoidance (no type-1 AGNs with $\text{FWHM} < 1000 \text{ km s}^{-1}$) and self-correlation. The dotted line indicates the upper envelope of the distribution defined by AGNs with $\text{FWHM} = 1000 \text{ km s}^{-1}$ for a fixed luminosity, $L_{5100} = 10^{44.5}$ and 10^{45} , respectively.

FWHM of the broad $H\beta$ line less than 1000 km s^{-1} (see the dashed line in Figure 19). For example, for a fixed AGN luminosity (i.e., $L_{5100} = 10^{45} \text{ erg s}^{-1}$) in the Eddington ratio between ~ 0.3 and 1, there is an upper envelope, above which no AGN can be located because the widths of the $H\beta$ broad-line are not typically smaller than 1000 km s^{-1} . Note that this effect is not strong at lower Eddington ratios (i.e., $< \sim 0.3$), leading to a negative correlation only at the high Eddington regime.

The decreasing trend, particularly at the high Eddington ratio is naturally expected (Figure 19 right) due to the self-correlation between the Eddington ratios and the deviation, since the former scales with L/R and the latter scales with $R/L^{0.5}$ as pointed out by Fonseca Alvarez et al. (2020). In other words, if the measured R_{BLR} is somewhat smaller than expected by the best fit, then the M_{BH} would be smaller. Consequently, the Eddington ratio of these targets would be systematically larger. Thus, the decreasing trend between the deviation and the Eddington ratio is expected due to the self-correlation.

To overcome these artificial trends due to the zone of avoidance and the self-correlation, we use the strength of Fe II emission (R_{Fe}), which is the ratio between the Fe II emission flux in the range of 4434-4684Å and the $H\beta$ emission flux, for comparing with the deviation (Figure 19 right). As R_{Fe} is closely related to Eigenvector 1 in PCA analyses of AGN properties, which is typically

interpreted as an accretion rate parameter, we use R_{Fe} as an indicator of Eddington ratio. Note that for this practice, we only use the subsample including SAMP, LAMP, and other AGNs with available R_{Fe} in the literature. However, we find no strong trend between the deviation from the size-luminosity relation and R_{Fe} , suggesting no systematic effect of accretion rate on the deviation from the BLR size. In contrast, SEAMBH project reported that the deviation of their sample correlated with dimensionless accretion rate (Du et al. 2014, 2015) as well as the FWHM/σ ratio of $H\beta$ line and R_{Fe} (Du et al. 2016; Du & Wang 2019). Note that we reproduce the same result as Du et al. (2016); Du & Wang (2019) using their sample. However, by adding more luminous sub-Eddington AGNs (e.g., SAMP AGNs), their correlation becomes weaker. We also note that by adopting a shallower slope of 0.4 in the size-luminosity relation, we obtain a systematically smaller correlation coefficient between the deviation and either R_{Fe} or Eddington ratio. A full analysis based on a large sample of reverberation-mapped AGNs with consistently measured $H\beta$ lag, line width, M_{BH} , and R_{Fe} is required to clearly investigate the dependency of the size-luminosity relation on the Eddington ratio. We will present more detailed results based on our re-analysis of $H\beta$ lag measurements and the size-luminosity relation using a large archival sample (Wang et al. in preparation).

5.1.3. What determines the slope of the size-luminosity relation?

In this section we discuss several scenarios to explain the observed slope of the $H\beta$ BLR size - optical luminosity relation. First, we expect that the BLR size is proportional to the 0.5 power of the ionizing luminosity if the ionization parameter (U) and hydrogen gas density (n_H) are similar for all AGNs, since U is proportional to $L_{\text{ion}}/(4\pi R^2 n_H)$, where L_{ion} is the photoionizing luminosity. However, this assumption may not be true as the gas clouds in the BLR could have a range of U and n_H (e.g., Baldwin et al. 1995). If higher luminosity AGNs have an average higher value of the product, $U \times n_H$, then the size of BLR gets smaller than expected, leading to a shallower slope. Currently, we do not have clear observational evidence for this trend.

Second, the optical luminosity measured at 5100\AA may not properly represent the ionizing luminosity although the UV continuum luminosity at around the Lyman edge may show a better correlation with a 0.5 slope (see discussion by Czerny et al. 2019; Fonseca Alvarez et al. 2020). In this scenario, the UV-to-optical flux ratio has to be systematically lower for higher luminosity AGNs, in order to be consistent with the observation that L_{5100} is larger than expected from the 0.5 slope for a given BLR size. Some of the thin disk models showed that the UV-to-optical flux ratio decreases with increasing bolometric luminosity, decreasing Eddington ratio, and decreasing black hole spin (e.g., Davis & Laor 2011; Castelló-Mor et al. 2016; Czerny et al. 2019). However, model predictions show various trends of the UV-to-optical flux ratio, depending on the model assumptions, i.e., radiative efficiency and wind (e.g., Laor & Davis 2014). In general, the UV-optical SED in the thin disk models is somewhat inconsistent with observations (e.g., Davis et al. 2007; Davis & Laor 2011). Clearly, more detailed studies are required to understand the effect on the spectral slope.

As an empirical test, we compare available $H\beta$ line luminosity with L_{5100} for a subsample of our collected $H\beta$ reverberation-mapped AGNs, finding a slightly sub-linear relation, $L_{H\beta} \propto (L_{5100})^{0.92 \pm 0.01}$ (Figure 20). If we assume $L_{H\beta}$ is proportional to the ionizing luminosity, we expect a ~ 0.46 slope in the BLR size - optical luminosity relation. These results suggest that the systematic change of the SED slope between UV and optical ranges may contribute to the deviation from the 0.5 slope by increasing L_{5100} for given BLR size and ionizing luminosity.

Third, super-Eddington AGNs may suffer a shortening of the BLR size owing to the self-shadowing effect of the slim disk as detailed by Wang et al. (2014). Gas clouds

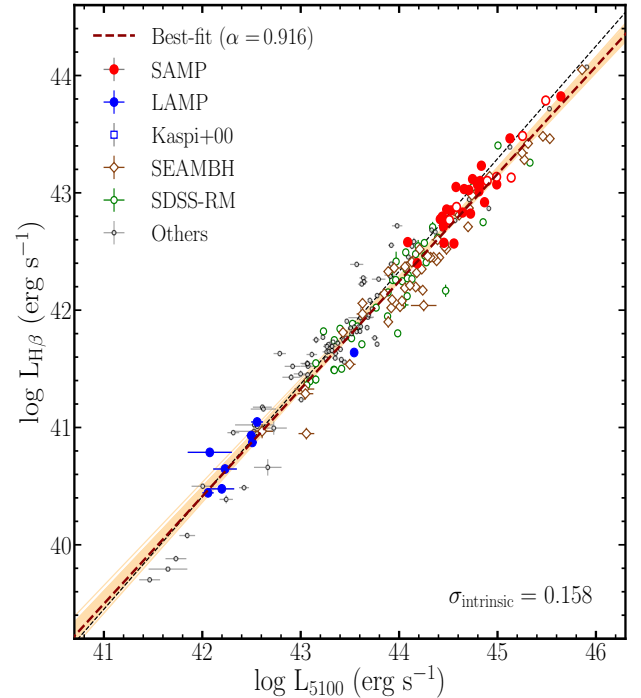


Figure 20. Comparison of the optical luminosity at 5100\AA with the $H\beta$ line luminosity for a subsample of the $H\beta$ reverberation AGNs.

in the BLR with a high inclination angle (with respect to the rotation axis) receive less ionizing photons than gas clouds with a lower inclination angle due to the shadowing of the funnel in the inner disk, and this effect in super-Eddington AGN leads to a shortening of the BLR size. Thus, super-Eddington AGNs have systematically smaller BLR sizes compared to sub-Eddington AGNs. Fourth, the BLR size-luminosity relation is driven by the outer boundary of the BLR, which is defined by the dust sublimation radius at the inner edge of the torus (Suganuma et al. 2006). Interestingly, the dust size - optical luminosity relation also shows a shallower slope than 0.5. For example, Minezaki et al. (e.g., 2019) reported a 0.424 slope between the K-band torus size and V-band continuum, and Amit et al. (2023 submitted) found a ~ 0.4 slope between the torus size based on the WISE W1-band and optical luminosity. Perhaps, this is also due to the self-shadowing effect of the slim disk model as pointed out by Chen et al. (2023).

We consider a sample selection effect of our collected AGNs. While we try to increase the number of high-luminosity AGNs in this study, there is also a lack of high Eddington ratio AGNs in the low-luminosity range. To demonstrate the difference in Eddington ratio distribution as a function of luminosity, we divide the sample

into 4 luminosity bins and present the Eddington ratio distribution in Figure 21. We clearly notice that the median Eddington ratio is increasing for higher luminosity bins. This trend can naturally cause the shallower slope if higher Eddington ratio AGNs tend to have smaller BLR sizes for given luminosity. In other words, a higher fraction of high Eddington ratio AGNs in higher luminosity bins can generate a shallower slope.

We discussed various effects, which could be responsible for the shallower slope of the correlation between the BLR size and optical luminosity. It is puzzling to observe a shortening of the BLR size for a given object. For example, the best-studied low-Eddington AGN, NGC 5548 showed a factor of 5-10 smaller BLR size for a given (or similar) optical luminosity (see Figure 13 in Pei et al. 2017). This suggests that the BLR size can change significantly without changing luminosity or Eddington ratio. More detailed studies are required to better understand the scatter and slope of the BLR size - luminosity relation.

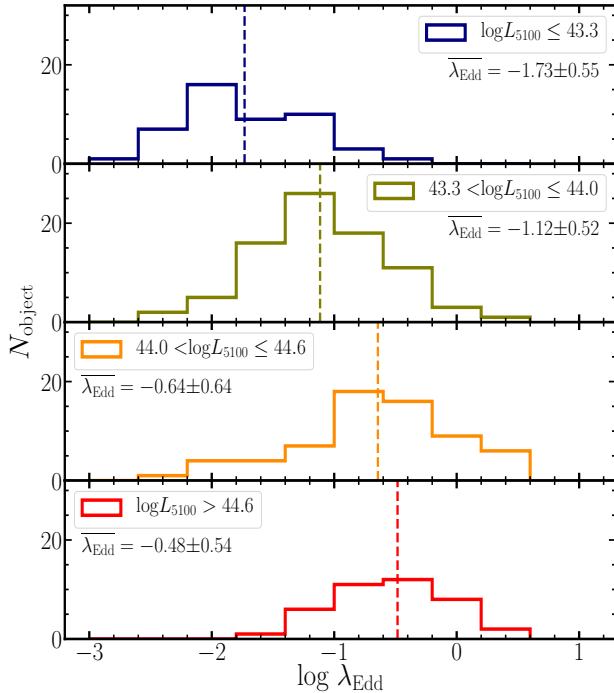


Figure 21. Eddington ratio distribution in each luminosity bin. It is clearly shown that higher luminosity bins contain on average higher Eddington ratio AGNs.

6. SUMMARY

We present $H\beta$ reverberation mapping results based on the six-year (2015-2021) data from the SNU AGN Monitoring Project. For a sample of 32 high luminosity

AGNs ($L_{5100,AGN} > 10^{44.1\sim 45.6}$ erg s $^{-1}$) at $z < \sim 0.4$, we measure the lags between the $H\beta$ and continuum light curves, using both the ICCF and JAVELIN methods. By applying three reliability parameters (r_{max} , $p(r_{max})$, and f_{peak}), we quantitatively access the lag measurements, and use the accepted measurements to investigate the BLR size-luminosity relation. Our main conclusions are:

1. Among the lag measurements of 32 targets, we report 25 best $H\beta$ lag measurements, which satisfy $r_{max} > 0.6$, $p(r_{max}) < 0.2$, and $f_{peak} < 0.6$. These new measurements significantly increase the current RM sample at high luminosity end.
2. We compare the JAVELIN lag τ_{JAV} with ICCF lag τ_{cent} , finding that they are generally consistent with each other but τ_{JAV} tends to systematically offset due to more alias. Thus, we adopt the ICCF τ_{cent} results as our final lag measurements.
3. By comparing the $H\beta$ BLR size and AGN continuum luminosity, we find that most of the SAMP AGNs are located below the previous relation measured by Bentz et al. (2013), suggesting that the slope is shallower than that expected from a simple photoionization model. We find the best slope of 0.39-0.46 by combining with previous $H\beta$ lag measurements in the literature. This result indicates that the single-epoch M_{BH} estimates based on the previous size-luminosity relation can be overestimated.
4. It is possible that the deviation from the size-luminosity relation correlates with Eddington ratio. However, we do not clearly confirm the correlation except for that caused by the self-correlation between AGN luminosity and Eddington ratio. Nevertheless, we detect a hint of correlation, using the Fe II relative strength. A consistent analysis of $H\beta$ lag and error measurements based on a uniform method for the large RM sample is necessary to unveil the nature of the size-luminosity relation.

While the sample size of the reverberation-mapped AGNs significantly increased over the last decade by various studies including the SAMP, there is a still scarcity of very high luminosity AGNs at $L_{5100} \sim 10^{46}$, and a uniform analysis including quantitative assessment of the measured lag is required to properly investigate the $H\beta$ BLR size-luminosity relation. These issues are beyond the scope of this paper and we will revisit them in the future.

J.-H.W. would like to thank all members of the SAMP for their efforts since 2015. We thank the anonymous

referee for her/his useful comments, which improved the presentation and clarity of the manuscript. J.-H.W. thanks Shane Davis and Omer Blaes for the discussion on the think disk models. This work has been supported by the Basic Science Research Program through the National Research Foundation (NRF) of Korean Government (2021R1A2C3008486) and the Samsung Science & Technology Foundation under Project Number SSTF-BA1501-05. S.W. acknowledges the support from the NRF grant funded by the Korean government (MEST) (No. 2019R1A6A1A10073437). M.K. was supported by the NRF grant (No. 2022R1A4A3031306) funded by the Korean government. Research at UCLA was supported by the NSF grant NSF-AST-1907208. Research at UC Irvine was supported by NSF grant AST-1907290. V.N.B. gratefully acknowledges assistance from NSF Research at Undergraduate Institutions (RUI) grant AST-1909297. Note that findings and conclusions do not necessarily represent views of the NSF. V.U acknowledges funding support from NASA Astrophysics Data Analysis Program (ADAP) grants #80NSSC20K0450 and #80NSSC23K0750, and Space Telescope Science Institute grants #HST-AR-17063.005-A, #HST-GO-17285.001, and #JWST-GO-01717.001. S.R. acknowledges the partial support of SRG-SERB, DST, New Delhi through grant no. SRG/2021/001334. H.A.N. Le acknowledges the support of the National Natural Science Foundation of China (NSFC-12003031) and the "Fundamental Research Funds for the Central Universities" We thank M. Fausnaugh for the advice in running `mapspec`, and Yanrong Li and Yu-yang Songsheng for installing `PyCALI`.

APPENDIX

A. RESULT OF NON-DETRENDING FOR PR1_ID19 AND PR1_ID27

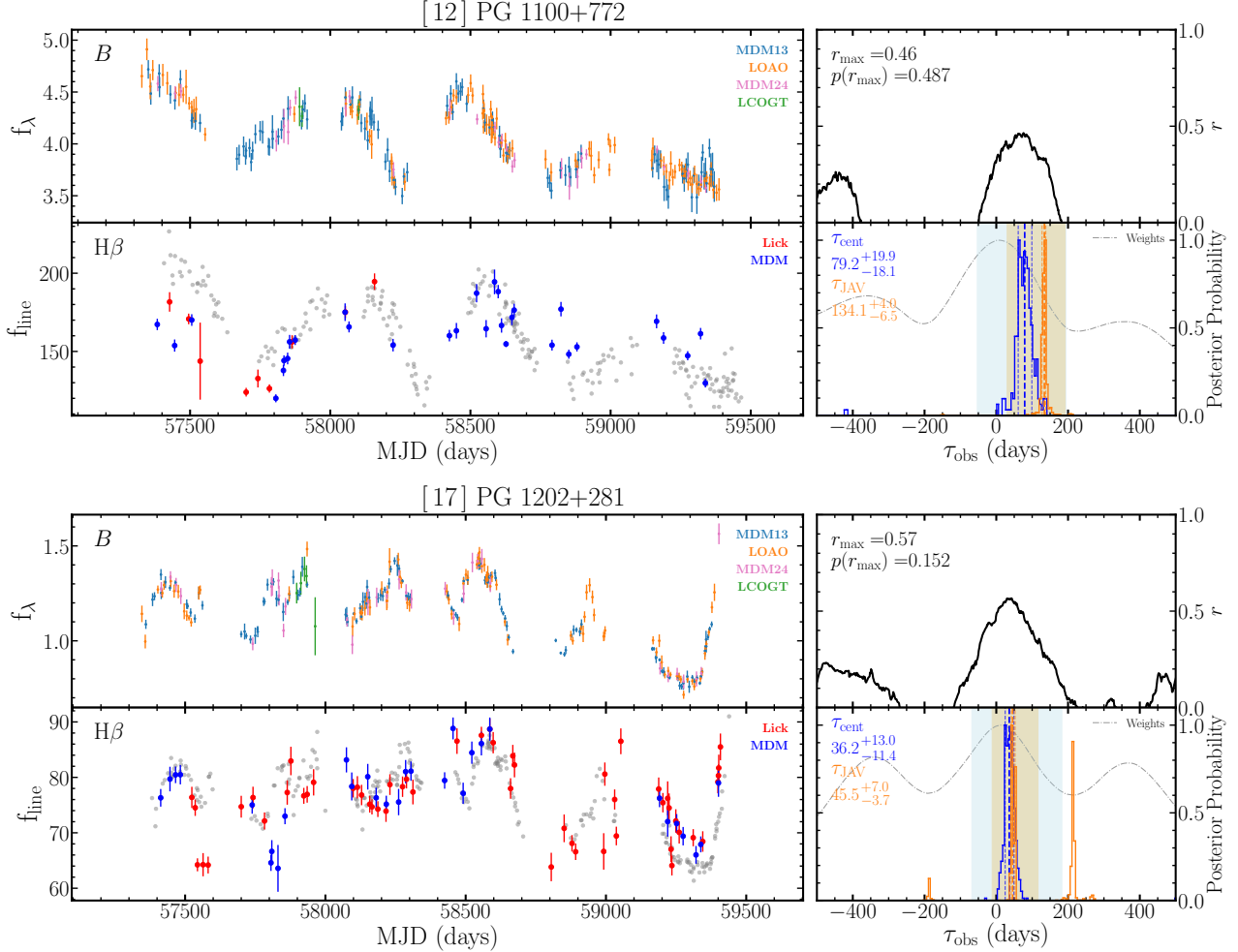


Figure A.1. The non-detrending lag estimation for PG 1100+772 and PG 1202+281. JAVELIN and p-value need to be updated.

B. COMPARISON WITH THE PREVIOUS MEASUREMENTS OF INDIVIDUAL OBJECTS

Mrk 1501: There were two previous monitoring campaigns of Mrk 1501 (Grier et al. 2012; Bao et al. 2022). Grier et al. (2012) observed this object from 2010 August to 2011 January and reported H β $\tau_{\text{cent}} = 12.6 \pm 3.9$ days in the rest-frame. Combining with the H β velocity dispersion measured from the rms spectrum, $\sigma_{\text{rms}} = 3321 \pm 107$ km/s, the BH mass was determined as $1.84 \pm 0.27 M_\odot$. In the case of the continuum luminosity, Dalla Bontà et al. (2020) reported $\log L_{5100, \text{AGN}} = 43.980 \pm 0.053$ based on the decomposition analysis with HST image. Our new measurements H β $\tau_{\text{cent}} = 11.7^{+7.6}_{-8.9}$ days and $\log L_{5100, \text{AGN}} = 44.09$ based on the SAMP data are generally consistent with Grier et al. (2012).

In addition, the target was observed from 2017 Oct. to 2021 Jan. by the Monitoring AGNs with H β Asymmetry project (MAHA, Du et al. 2018b; Brotherton et al. 2020; Bao et al. 2022). Note that their monitoring baseline is overlapped with the SAMP baseline between 2018 and 2021. They reported H β $\tau_{\text{cent}} = 30.9^{+2.5}_{-2.4}$ days ($\tau_{\text{MICA}} = 25.8^{+1.2}_{-1.1}$ days) using all seasons, while using the 2020 data they measured H β $\tau_{\text{cent}} = 15.6^{+15.4}_{-11.1}$ days, which is in agreement with our measurement. Mrk 1501 is located below the best-fit slope of the size-luminosity relation by 0.41 dex. Since this

object is a radio-loud AGN with strong radio variability (e.g., Unger et al. 1987), a possible scenarios is that the jet contribution to the optical luminosity may cause an overestimation of the continuum luminosity and underestimation of the H β lag. Further study is required to investigate this effect.

PG 0026+129: There were two previous monitoring campaigns of PG 0026+129 (Kaspi et al. 2000; Hu et al. 2020). Kaspi et al. (2000) observed the target during a ~ 7 year campaign, and Peterson et al. (2004) reanalyzed the data, reporting H β $\tau_{\text{cent}} = 111.0_{-28.3}^{+24.1}$ days in the observed frame. In contrast, Hu et al. (2020) found a much smaller H β lag based on a much higher cadence monitoring campaign as H β $\tau_{\text{cent}} = 11.7_{-7.8}^{+7.4}$ days and H β $\tau_{\text{cent}} = 27.7_{-6.0}^{+5.0}$ days using 2017 and 2019 data, respectively. While the baseline of their campaign overlapped with that of the SAMP, our data with lower cadence and smaller number of epochs could not provide a good temporal coverage. Thus, we removed this target from our measurements (i.e., H β lag was comparable to 0 within the uncertainty).

PG 0052+251: Kaspi et al. (2000) observed PG 0052+251 from 1991 July to 1998 September and Peterson et al. (2004) reanalyzed the data, reporting the rest-frame H β $\tau_{\text{cent}} = 89.8_{-24.1}^{+24.5}$ days. Our new measurement $\tau_{\text{cent}} = 63.9_{-10.9}^{+12.0}$ days is smaller but consistent with their lag within uncertainties. In the case of the continuum luminosity, our estimate $\log L_{5100, \text{AGN}} = 44.75 \pm 0.01$ is comparable with $\log L_{5100, \text{AGN}} = 44.791 \pm 0.020$ based on the HST imaging analysis by (Dalla Bontà et al. 2020).

PG 0947+397: PG 0947+397 was monitored by the MAHA from 2017 October to 2021 May, which overlapped with the SAMP's baseline from 2018 to 2021. Bao et al. (2022) reported H β lag $\tau_{\text{cent}} = 34.4_{-4.9}^{+4.5}$ days in the rest-frame, consistent with ours within 1σ .

PG 1100+772: PG 1100+772 was monitored by MAHA from 2018 November to 2021 April which overlapped with SAMP's baseline from 2018 to 2021. They reported H β lag $\tau_{\text{cent}} = 44.9_{-30.8}^{+30.5}$ days in the rest-frame. Our new lag measurement is well consistent with theirs within 1σ uncertainty with slightly smaller uncertainties due to longer baseline. We find that the rms FWHM and σ_{line} in Bao et al. (2022) were reported to be 11229_{-23}^{+29} and 4002_{-110}^{+87} km/s, respectively, which is much higher than our measurements. As a consequence, their derived M_{BH} ($78.13_{-4.72}^{+5.44} \times 10^7 M_{\odot}$) is much larger than ours ($2.8_{-1.2}^{+0.8} \times 10^8 M_{\odot}$). We suggest that the difference is a result of the line variability between the different time baseline. As the line variability in 2016 and 2017 are larger than that of the following three years, the width of the rms line profile based on the six-year data becomes smaller. Note that the line widths measured from mean spectra show more consistency between the two studies. This object is very interesting as it is a strong outlier of $R-L$ relation but its low R_{Fe} and strong [O III]/H β ratio indicates that it is not a typical SEAMBHs.

PG 1202+281: PG 1202+281 was monitored by MAHA from 2016 December to 2021 April which overlapped with the SAMP's baseline from 2018 to 2021. They reported H β lag $\tau_{\text{cent}} = 98.5_{-30.1}^{+28.2}$ days in the rest-frame together with a total $L_{5100} = 3.42 \pm 0.32 \times 10^{44}$ erg/s (Bao et al. 2022). Our new measurement ($38.5_{-8.5}^{+9.1}$) is much smaller but still consistent with 3σ uncertainties. Note that their lag measurement of individual season in 2018 and 2020, i.e., $50.0_{-4.6}^{+6.6}$ and $53.3_{-8.5}^{+10.9}$ days, respectively, is much closer to our values. Our derived luminosity is slightly lower than theirs that can also partly explain the difference. Combining with the measured rms FWHM and σ_{line} (4255_{-17}^{+23} and 1301_{-24}^{+18} km/s, respectively), which is much smaller than our values (5545 ± 62 and 2186 ± 25 km/s respectively), they derived a $M_{\text{BH}} = 9.80_{-0.46}^{+0.44} \times 10^7 M_{\odot}$, close to our measurements ($1.2_{-0.3}^{+0.3} \times 10^8 M_{\odot}$).

REFERENCES

- Alexander, T. 2013, arXiv e-prints, arXiv:1302.1508
- Arévalo, P., Uttley, P., Kaspi, S., et al. 2008, MNRAS, 389, 1479
- Baldwin, J., Ferland, G., Korista, K., & Verner, D. 1995, ApJL, 455, L119
- Bao, D.-W., Brotherton, M. S., Du, P., et al. 2022, arXiv e-prints, arXiv:2207.00297
- Barth, A. J., Sarzi, M., Rix, H.-W., et al. 2001, ApJ, 555, 685
- Barth, A. J., Bennert, V. N., Canalizo, G., et al. 2015, ApJS, 217, 26
- Bentz, M. C., Peterson, B. M., Netzer, H., Pogge, R. W., & Vestergaard, M. 2009a, ApJ, 697, 160
- Bentz, M. C., Walsh, J. L., Barth, A. J., et al. 2009b, ApJ, 705, 199
- Bentz, M. C., Denney, K. D., Grier, C. J., et al. 2013, ApJ, 767, 149
- Bertin, E., & Arnouts, S. 1996, A&AS, 117, 393
- Bertin, E., Mellier, Y., Radovich, M., et al. 2002, in Astronomical Society of the Pacific Conference Series, Vol. 281, Astronomical Data Analysis Software and Systems XI, ed. D. A. Bohlender, D. Durand, & T. H. Handley, 228
- Blandford, R. D., & McKee, C. F. 1982, ApJ, 255, 419
- Boizelle, B. D., Walsh, J. L., Barth, A. J., et al. 2021, ApJ, 908, 19

- Boroson, T. A., & Green, R. F. 1992, *ApJS*, 80, 109
- Brotherton, M. S., Du, P., Xiao, M., et al. 2020, *ApJ*, 905, 77
- Bruzual, G., & Charlot, S. 2003, *MNRAS*, 344, 1000
- Castelló-Mor, N., Netzer, H., & Kaspi, S. 2016, *MNRAS*, 458, 1839
- Chatterjee, R., Jorstad, S. G., Marscher, A. P., et al. 2008, *ApJ*, 689, 79
- Chen, Y.-J., Liu, J.-R., Zhai, S., et al. 2023, *MNRAS*, 522, 3439
- Cho, H., Woo, J.-H., Wang, S., et al. 2023, *ApJ*, 953, 142
- Collin, S., Kawaguchi, T., Peterson, B. M., & Vestergaard, M. 2006, *A&A*, 456, 75
- Czerny, B., Wang, J.-M., Du, P., et al. 2019, *ApJ*, 870, 84
- Dalla Bontà, E., Peterson, B. M., Bentz, M. C., et al. 2020, *ApJ*, 903, 112
- Davies, R. I., Thomas, J., Genzel, R., et al. 2006, *ApJ*, 646, 754
- Davis, S. W., & Laor, A. 2011, *ApJ*, 728, 98
- Davis, S. W., Woo, J.-H., & Blaes, O. M. 2007, *ApJ*, 668, 682
- den Brok, M., Seth, A. C., Barth, A. J., et al. 2015, *ApJ*, 809, 101
- Denney, K. D., Peterson, B. M., Pogge, R. W., et al. 2010, *ApJ*, 721, 715
- Du, P., & Wang, J.-M. 2019, *ApJ*, 886, 42
- Du, P., Hu, C., Lu, K.-X., et al. 2014, *ApJ*, 782, 45
- . 2015, *ApJ*, 806, 22
- Du, P., Lu, K.-X., Zhang, Z.-X., et al. 2016, *ApJ*, 825, 126
- Du, P., Zhang, Z.-X., Wang, K., et al. 2018a, *ApJ*, 856, 6
- Du, P., Brotherton, M. S., Wang, K., et al. 2018b, *ApJ*, 869, 142
- Edelson, R., Turner, T. J., Pounds, K., et al. 2002, *ApJ*, 568, 610
- Edelson, R. A., & Krolik, J. H. 1988, *ApJ*, 333, 646
- Event Horizon Telescope Collaboration, Akiyama, K., Alberdi, A., et al. 2019, *ApJL*, 875, L1
- . 2022, *ApJL*, 930, L12
- Fausnaugh, M. M. 2017, *PASP*, 129, 024007
- Flesch, E. W. 2015, *PASA*, 32, e010
- Fonseca Alvarez, G., Trump, J. R., Homayouni, Y., et al. 2020, *ApJ*, 899, 73
- Gaskell, C. M., & Peterson, B. M. 1987, *ApJS*, 65, 1
- Grier, C. J., Peterson, B. M., Pogge, R. W., et al. 2012, *ApJ*, 755, 60
- Grier, C. J., Trump, J. R., Shen, Y., et al. 2017, *ApJ*, 851, 21
- Grier, C. J., Shen, Y., Horne, K., et al. 2019, *ApJ*, 887, 38
- Gültekin, K., Richstone, D. O., Gebhardt, K., et al. 2009, *ApJ*, 698, 198
- Guo, H., & Barth, A. J. 2021, in *American Astronomical Society Meeting Abstracts*, Vol. 53, American Astronomical Society Meeting Abstracts, 226.08
- Homayouni, Y., Trump, J. R., Grier, C. J., et al. 2020, *ApJ*, 901, 55
- Hu, C., Du, P., Lu, K.-X., et al. 2015, *ApJ*, 804, 138
- Hu, C., Li, S.-S., Guo, W.-J., et al. 2020, *ApJ*, 905, 75
- Hu, C., Li, S.-S., Yang, S., et al. 2021, *ApJS*, 253, 20
- Jha, V. K., Joshi, R., Chand, H., et al. 2022, *MNRAS*, 511, 3005
- Kabasares, K. M., Barth, A. J., Buote, D. A., et al. 2022, *ApJ*, 934, 162
- Kaspi, S., Smith, P. S., Netzer, H., et al. 2000, *ApJ*, 533, 631
- Kelly, B. C., Bechtold, J., & Siemiginowska, A. 2009, *ApJ*, 698, 895
- Kovačević, J., Popović, L. Č., & Dimitrijević, M. S. 2010, *ApJS*, 189, 15
- Lang, D., Hogg, D. W., Mierle, K., Blanton, M., & Roweis, S. 2010, *The Astronomical Journal*, 139, 1782.
<https://dx.doi.org/10.1088/0004-6256/139/5/1782>
- Laor, A., & Davis, S. W. 2014, *MNRAS*, 438, 3024
- Li, I-Hsiu, J., Shen, Y., Brandt, W. N., et al. 2019, *ApJ*, 884, 119
- Li, S.-S., Yang, S., Yang, Z.-X., et al. 2021, *ApJ*, 920, 9
- Li, Y.-R., Wang, J.-M., & Bai, J.-M. 2016, *ApJ*, 831, 206
- Li, Y.-R., Wang, J.-M., Hu, C., Du, P., & Bai, J.-M. 2014, *ApJL*, 786, L6
- Li, Y.-R., Zhang, Z.-X., Jin, C., et al. 2020, *ApJ*, 897, 18
- MacLeod, C. L., Ivezić, Ž., Kochanek, C. S., et al. 2010, *ApJ*, 721, 1014
- Malik, U., Sharp, R., Penton, A., et al. 2022, *arXiv e-prints*, arXiv:2210.03977
- Marconi, A., Axon, D. J., Capetti, A., et al. 2003, *ApJ*, 586, 868
- Martínez-Aldama, M. L., Czerny, B., Kawka, D., et al. 2019, *ApJ*, 883, 170
- Minezaki, T., Yoshii, Y., Kobayashi, Y., et al. 2019, *ApJ*, 886, 150
- Netzer, H. 2022, *MNRAS*, 509, 2637
- Oke, J. B. 1990, *AJ*, 99, 1621
- Onken, C. A., Ferrarese, L., Merritt, D., et al. 2004, *ApJ*, 615, 645
- Pancoast, A., Brewer, B. J., & Treu, T. 2011, *ApJ*, 730, 139
- . 2014a, *MNRAS*, 445, 3055
- Pancoast, A., Brewer, B. J., Treu, T., et al. 2014b, *MNRAS*, 445, 3073
- Pancoast, A., Skielboe, A., Pei, L., et al. 2019, *ApJ*, 871, 108

- Park, D., Kelly, B. C., Woo, J.-H., & Treu, T. 2012a, *ApJS*, 203, 6
- Park, D., Woo, J.-H., Treu, T., et al. 2012b, *ApJ*, 747, 30
- Park, S., Woo, J.-H., Romero-Colmenero, E., et al. 2017, *ApJ*, 847, 125
- Pei, L., Fausnaugh, M. M., Barth, A. J., et al. 2017, *ApJ*, 837, 131
- Peterson, B. M. 1993, *PASP*, 105, 247
- Peterson, B. M., Pogge, R. W., Wanders, I., Smith, S. M., & Romanishin, W. 1995, *PASP*, 107, 579
- Peterson, B. M., Wanders, I., Horne, K., et al. 1998, *PASP*, 110, 660
- Peterson, B. M., Ferrarese, L., Gilbert, K. M., et al. 2004, *ApJ*, 613, 682
- Prochaska, J., Hennawi, J., Westfall, K., et al. 2020a, *The Journal of Open Source Software*, 5, 2308
- Prochaska, J. X., Hennawi, J., Cooke, R., et al. 2020b, *pypeit/PypeIt: Release 1.0.0*, Zenodo, vv1.0.0, Zenodo, doi:10.5281/zenodo.3743493
- Rakshit, S., Woo, J.-H., Gallo, E., et al. 2019, *ApJ*, 886, 93
- Richards, G. T., Strauss, M. A., Fan, X., et al. 2006, *AJ*, 131, 2766
- Rodríguez-Pascual, P. M., Alloin, D., Clavel, J., et al. 1997, *ApJS*, 110, 9
- Sánchez-Sáez, P., Lira, H., Martí, L., et al. 2021, *AJ*, 162, 206
- Scharwächter, J., McGregor, P. J., Dopita, M. A., & Beck, T. L. 2013, *MNRAS*, 429, 2315
- Schlafly, E. F., & Finkbeiner, D. P. 2011, *ApJ*, 737, 103
- Shen, Y., & Liu, X. 2012, *ApJ*, 753, 125
- Shen, Y., Richards, G. T., Strauss, M. A., et al. 2011, *ApJS*, 194, 45
- Shen, Y., Horne, K., Grier, C. J., et al. 2016, *ApJ*, 818, 30
- Shen, Y., Hall, P. B., Horne, K., et al. 2019, *ApJS*, 241, 34
- Starkey, D. A., Horne, K., & Villforth, C. 2016, *MNRAS*, 456, 1960
- Suganuma, M., Yoshii, Y., Kobayashi, Y., et al. 2006, *ApJ*, 639, 46
- Sun, M., Xue, Y., Richards, G. T., et al. 2018, *ApJ*, 854, 128
- Tody, D. 1986, in *Society of Photo-Optical Instrumentation Engineers (SPIE) Conference Series*, Vol. 627, *Instrumentation in astronomy VI*, ed. D. L. Crawford, 733
- Tody, D. 1993, in *Astronomical Society of the Pacific Conference Series*, Vol. 52, *Astronomical Data Analysis Software and Systems II*, ed. R. J. Hanisch, R. J. V. Brissenden, & J. Barnes, 173
- U, V., Barth, A. J., Vogler, H. A., et al. 2022, *ApJ*, 925, 52
- Unger, S. W., Lawrence, A., Wilson, A. S., Elvis, M., & Wright, A. E. 1987, *MNRAS*, 228, 521
- Uttley, P., Edelson, R., McHardy, I. M., Peterson, B. M., & Markowitz, A. 2003, *ApJL*, 584, L53
- van Dokkum, P. G. 2001, *PASP*, 113, 1420
- van Groningen, E., & Wanders, I. 1992, *PASP*, 104, 700
- Vestergaard, M., & Peterson, B. M. 2006, *ApJ*, 641, 689
- Villafaña, L., Williams, P. R., Treu, T., et al. 2022, *ApJ*, 930, 52
- Wandel, A., Peterson, B. M., & Malkan, M. A. 1999, *ApJ*, 526, 579
- Wang, J.-M., Du, P., Hu, C., et al. 2014, *ApJ*, 793, 108
- Wang, S., Guo, H., & Woo, J.-H. 2023, *ApJL*, 948, L23
- Wang, S., Shen, Y., Jiang, L., et al. 2019, *ApJ*, 882, 4
- Welsh, W. F. 1999, *PASP*, 111, 1347
- White, R. J., & Peterson, B. M. 1994, *PASP*, 106, 879
- Williams, P. R., Pancoast, A., Treu, T., et al. 2018, *ApJ*, 866, 75
- Woo, J.-H., & Urry, C. M. 2002, *ApJ*, 579, 530
- Woo, J.-H., Yoon, Y., Park, S., Park, D., & Kim, S. C. 2015, *ApJ*, 801, 38
- Woo, J.-H., Treu, T., Barth, A. J., et al. 2010, *ApJ*, 716, 269
- Woo, J.-H., Son, D., Gallo, E., et al. 2019, *Journal of Korean Astronomical Society*, 52, 109
- Yu, Z., Martini, P., Penton, A., et al. 2022, *arXiv e-prints*, arXiv:2208.05491
- Zhang, Z.-X., Du, P., Smith, P. S., et al. 2019, *ApJ*, 876, 49
- Zu, Y., Kochanek, C. S., & Peterson, B. M. 2011, *ApJ*, 735, 80